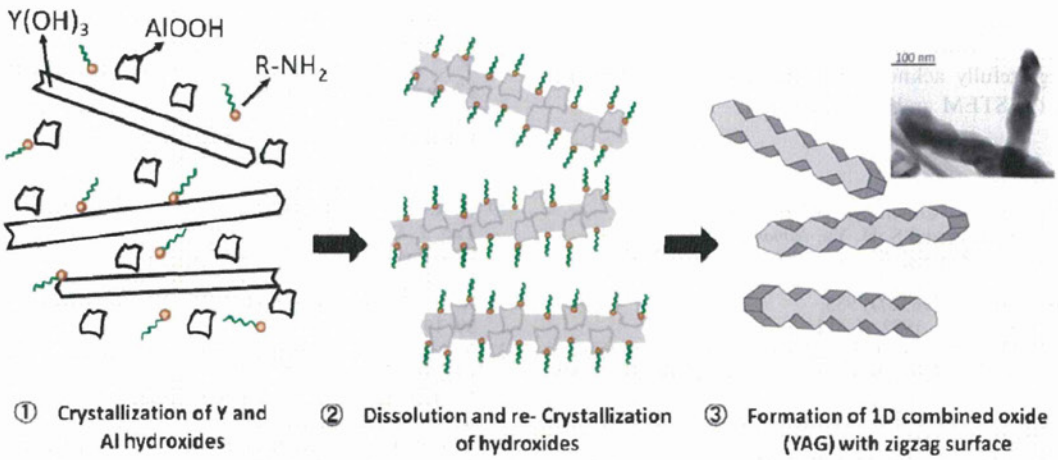

Scheme 1 Formation of 1D YAG nanostructures *via* preferential attachment of organic amines.

changes in the acidity of the different crystal planes of sapphire as a function of crystal orientation by the streaming potential technique. They proposed that the structural and electronic characteristics of crystallographic surfaces are responsible for determining their acidities.[48] Bullard and Cima reported the same phenomena for the different crystallographic facets of TiO_2 (rutile). Their studies also showed a strong dependence of the surface potential and colloidal interactions on the atomic structure of crystallographic surfaces.[49] In both studies, the coordination of the atoms existing on the crystallographic surfaces was highlighted as an important structural parameter governing surface acidities. Those planes, which are composed of the higher number of coordinated cations exhibit weaker attraction to absorbed hydroxyl ions, whereas planes composed of less-coordinated cations may exhibit the most acidic behavior.

We believe that similar phenomena occur during the formation of the 1D YAG nanostructures. During the hydrothermal reaction, when the reaction pH is less than the dissociation constant of the alkylamine molecules ($pH<pK_b$), these molecules can dissociate and be protonated to form $R–NH_3^+$ ions. When an acidic precursor (pH = 5.5) is used, the crystallographic planes carry positive charges. Therefore, there will be repulsive forces between the positively charged surfaces and the NH_3^+ ions. Under such conditions, the amine molecules cannot attach to the surface of the YAG crystals in order to control their growth and surface properties. As a result, the particles are mostly aggregated. Alternatively, when a highly alkaline precursor with pH = 12.5 is used, almost all crystallographic planes are negatively charged owing to the existence of sufficient OH^- ions in the reaction medium. Under these conditions, preferential attraction of NH_3^+ ions toward crystal surfaces would not exist. Therefore, crystal growth is controlled in all crystallographic directions, and thus, semispherical particles are obtained under these conditions.

However, when a precursor of moderate pH (9.95) is used, some crystallographic planes can be negatively charged, depending on their degree of acidity. Therefore, NH_3^+ ions will be electrostatically attracted to these planes, thus hindering plane growth. On the other hand, the <001> planes might not be able to carry negative charges. Comparison of the atomic orientation of a cubic YAG crystals along different crystallographic planes[50] revealed that the <001> planes have the largest number of under-coordinated atoms compared with the other planes. This result supports the theory proposed in ref. 48 and 49 that such planes have the least tendency to adsorb OH^- ions and become negatively charged. Hence, the amine molecules cannot attach to this plane, and plane growth continues until the final 1D nanostructures are formed.

One of the most important applications of YAG NPs is the fabrication of high-performance lasers designed for use in optical nanodevices. We believe that for such applications, our new 1D YAG nanostructures could be better candidates for producing aligned nanostructures and achieving better control of the flow of light in lasing materials.

Conclusion

In the present study, novel 1D YAG nanostructures with zigzag surfaces were synthesized within 10 min in supercritical water in the presence of alkyl amines. The XRD pattern of the obtained products showed that all structures were pure YAG with a cubic crystal phase. According to the NBD patterns, the synthesized nanostructures exhibited a single crystalline nature and grew preferentially along the <001> direction. A systematic study was conducted to elucidate the formation mechanism of the 1D nanostructures. For this purpose, the effect of different reaction parameters such as the presence of organic capping agents, concentration of OH^- ions, and the state of water (sub- or supercritical conditions) were investigated. The results showed that the simultaneous influence of the above-mentioned parameters contributed to anisotropic crystal growth and the formation of the nanostructures. It was speculated that according to the different acidities of the crystallographic planes, certain crystal facets were negatively charged due to OH^- ions. This negative charge resulted in electrostatic attraction of NH_2 groups toward those facets; the NH_2 groups were protonated to NH^{3+} ions under hydrothermal conditions. Therefore, the growth of those facets was halted, whereas crystal growth continued along the remaining free crystal facets.

Acknowledgements

The authors gratefully acknowledge Mr. Takamichi Miyazaki for obtaining the STEM and EDX results.

References

1 W. E. Buhro and V. L. Colvin, *Nat. Mater.*, 2003, **2**, 138.
2 H. B. Yao, M. R. Gao and S. H. Yu, *Nanoscale*, 2010, **2**, 323.
3 J. L. Marignier, J. Belloni, M. O. Delcourt and J. P. Chevalier, *Nature*, 1985, **317**, 344.
4 P. Alivisatos, *Science*, 1996, **271**, 933.
5 G. A. Ozin, *Adv. Mater.*, 1992, **4**, 612.
6 Y. W. Jun, Y. M. Huh, J. S Choi, J. H. Lee, H. T Song, S. Kim, S. Yoon, K. S. Kim, J. S. Shin and J. Cheon, *J. Am. Chem. Soc.*, 2005, **127**, 5732.
7 D. Kimberly, T. Dhanasekaran, Z. Zhang and D. Meisel, *J. Am. Chem. Soc.*, 2002, **124**, 2312.
8 Y. Li, F. Qian, J. Xiang and C. M. Lieber, *Mater. Today*, 2006, **9**, 18.
9 C. Thelander, P. Agarwal, S. Brongersma, J. Eymery, L. F. Feiner, A. Forchel, M. Scheffler, W. Riess, B. J. Ohlsson, U. Gösele and L. Samuelson, *Mater. Today*, 2006, **9**, 28.
10 D. Gu, H. Baumgart, K. Tapily, P. Shrestha, G. Namkoong, X. Ao and F. Müller, *Nano Res.*, 2011, **4**, 164.
11 C. Thelander, P. Agarwal, S. Brongersma, J. Eymery, L. F. Feiner, A. Forchel, M. Scheffler, W. Riess, B. J. Ohlsson, U. Gosele and L. Samuelson, *Mater. Today*, 2006, **9**, 28.
12 Y. Li, F. Qian, J. Xiang and C. M. Lieber, *Mater. Today*, 2006, **9**, 18.
13 Y. Xia, P. Yang, Y. Sun, Y. Wu, B. Mayers, B. Gates, Y. Yin, F. Kim and H. Yan, *Adv. Mater.*, 2003, **15**, 353.
14 K. Kim, T. Moon, J. Kim and S. Kim, *Nanotechnology*, 2011, **22**, 245203.
15 M. K. Devaraju, S. Yin and T. Sato, *Nanotechnology*, 2009, **20**, 305302.
16 G. Jia, Y. Huang, Y. Song, M. Yang and L. Zhang, *Eur. J. Inorg. Chem.*, 2009, 3721. [Remark 3].
17 Y. L. Cao, Z. T. Liu, L. M. Chen, Y. B. Tang, L. B. Luo, J. S. Jie, W. J. Zhang, S. T. Lee and C. S. Lee, *Opt. Express*, 2011, **19**, 6100.
18 D. Vanmaekelbergh and L. K. Vugt, *Nanoscale*, 2011, **3**, 2783.
19 H. W. Liang, S. Liu and S. H. Yu, *Adv. Mater.*, 2010, **22**, 3925.
20 H. B. Yao, M. R. Gao and S. H. Yu, *Nanoscale*, 2010, **2**, 323.
21 G. Wei, C. W. Nan, Y. Deng and Y. H. Lin, *Chem. Mater.*, 2003, **15**, 4436.
22 Y. Deng, G. D. Wei and C. W. Nan, *Chem. Phys. Lett.*, 2003, **368**, 639.
23 Z. Zhong, M. Lin, V. Ng, G. X. B. Ng, Y. Foo and A. Gedanken, *Chem. Mater.*, 2006, **18**, 6031.
24 Y. Xia, P. Yang, Y. Sun, Y. Wu, B. Mayers, B. Gates, Y. Yin, F. Kim and H. Yan, *Adv. Mater.*, 2003, **15**, 353.
25 A. Sahraneshin, S. Takami, K. Minami, D. Hojo, T. Arita and T. Adschiri, *Prog. Cryst. Growth Charact. Mater.*, 2012, **58**, 43.
26 Y. C. Kang, I. W. Lenggoro, S. B. Park and K. Okuyama, *J. Phys. Chem. Solids*, 1999, **60**, 1855.
27 A. Cabanas, J. Li, P. Blood, T. Chudobac, W. Lojkowski, M. Poliakoff and E. Lester, *J. Supercrit. Fluids*, 2007, **40**, 284.
28 L. Mancic, K. Marinkovic, B. A. Marinkovic, M. Dramicanin and O. Milosevic, *J. Eur. Ceram. Soc.*, 2010, **30**, 577.
29 Q. X. Zheng, B. Li, H. D. Zhang, J. J. Zheng, M. H. Jiang and X. T. Tao, *J. Supercrit. Fluids*, 2009, **50**, 77.
30 A. Purwanto, W. N. Wang, T. Ogi, I. W. Lenggoro, E. Tanabe and K. Okuyama, *J. Alloys Compd.*, 2008, **1,2**, 350.
31 X. Li, H. Liu, J. Wang, H. Cui and F. Han, *Mater. Res. Bull.*, 2004, **39**, 1923.
32 X. Li, H. Liu, J. Wang, H. Cui, F. Han and R. I. Boughton, *J. Am. Ceram. Soc.*, 2004, **87**, 2288.
33 Y. H. Zhou, J. Lin, M. Yu, S. M. Han, S. B. Wang and H. J. Zhang, *Mater. Res. Bull.*, 2003, **38**, 1289.
34 Y. Hakuta, T. Haganuma, K. Sue, T. Adschiri and K. Arai, *Mater. Res. Bull.*, 2003, **38**, 1257.
35 Y. Li, M. Sui, Y. Ding, G. Zhang, J. Zhuang and C. Wang, *Adv. Mater.*, 2000, **12**, 818.
36 D. Chen and Y. Sugahara, *Chem. Mater.*, 2007, **19**, 1808.
37 J. Zhang, K. Sun, A. Kumbhar and J. Fang, *J. Phys. Chem. C*, 2008, **112**, 5454.
38 Y. Hakuta, K. Seino, H. Ura, T. H. Takizawa and K. Arai, *J. Mater. Chem.*, 1999, **9**, 2671.
39 Y. W Jun, J. H. Lee, J. S. Choi and J. Cheon, *J. Phys. Chem. B*, 2005, **109**, 14795.
40 X. Peng, L. Manna, W. Yang, J. Wickham, E. Scher, A. Kadavanich and A. P. Alivisatos, *Nature*, 2000, **404**, 59.
41 Y. Sun and Y. Xia, *Science*, 2002, **298**, 2176.
42 L. Manna, E. C. Scher, L. S. Li and A. P. Alivisatos, *J. Am. Chem. Soc.*, 2002, **124**, 7136.
43 J. Wang, X. Wang, W. Lou and W. Liu, *Mater. Res. Bull.*, 2010, **45**, 772.
44 B. Xi, S. Xiong, H. Fan, X. Wang and Y. Qian, *Cryst. Growth Des.*, 2007, **7**, 1185.
45 S. M. Lee, Y. Jun, S. N. Cho and J. Cheon, *J. Am. Chem. Soc.*, 2002, **124**, 11244.
46 J. Seo, Y. Jun, S. J. Ko and J. Cheon, *J. Phys. Chem. B*, 2005, **109**, 5389.
47 H. Ringsdorf, B. Schlarb and J. Venzmer, *Angew. Chem., Int. Ed. Engl.*, 1988, **27**, 113.
48 R. J. Kershner, J. W. Bullard and M. J. Cima, *Langmuir*, 2004, **20**, 4101.
49 J. W. Bullard and M. J. Cima, *Langmuir*, 2006, **22**, 10264.
50 Ł. Dobrzycki, E. Bulska, D. A. Pawlak, Z. Frukacz and K. Woz'niak, *Inorg. Chem.*, 2004, **43**, 7656.

AIP | Journal of Applied Physics

The assembly of kinesin-based nanotransport systems

D. Oliveira, D.-M. Kim, M. Umetsu, I. Kumagai, T. Adschiri et al.

Citation: J. Appl. Phys. **112**, 124703 (2012); doi: 10.1063/1.4769870
View online: http://dx.doi.org/10.1063/1.4769870
View Table of Contents: http://jap.aip.org/resource/1/JAPIAU/v112/i12
Published by the American Institute of Physics.

JOURNAL OF APPLIED PHYSICS **112**, 124703 (2012)

The assembly of kinesin-based nanotransport systems

D. Oliveira,[1] D.-M. Kim,[2] M. Umetsu,[1,2] I. Kumagai,[2] T. Adschiri,[1] and W. Teizer[1,3,a)]
[1]*World Premier International—Advanced Institute for Materials Research, Tohoku University, 2-1-1 Katahira, Aoba-ku, Sendai 980-8577, Japan*
[2]*Department of Biomolecular Engineering, Tohoku University, 6-6-07, Aoba-yama, Aoba-ku, Sendai 980-8579, Japan*
[3]*Department of Physics and Astronomy, Texas A&M University, College Station, Texas 77843-4242, USA*

(Received 20 July 2012; accepted 19 November 2012; published online 19 December 2012)

At the nano-scale many proteins act as biological actuators for rotation or translation. Among these proteins, the building blocks of self-assembled, highly efficient natural motors, kinesin is considered a promising tool in the development of synthetic nanorobots. Conversion of chemical energy into mechanical work, harnessed by the hydrolysis of adenosine triphosphate, propels kinesin along a cytoplasmic system of fibers, known as a microtubule. Even though recent efforts were made to engineer tailor-made artificial nanotransport systems using kinesin, no systematic study investigated how these systems can be organized from the bottom up using the surface plasmon resonance technique. Here, we show that it is possible to quantitatively evaluate how each component of such nanoscopic machines is sequentially assembled by monitoring the individual association of its components, focusing specifically on the kinesin association to microtubules as well as the cargo-kinesin association. Furthermore, the kinetic parameters reported here for the microtubules and recombinant biotinylated kinesin binding process properties are of utmost importance due to the current widespread use of biotinylated kinesin in the construction of synthetic nano-machines. © *2012 American Institute of Physics*. [http://dx.doi.org/10.1063/1.4769870]

I. INTRODUCTION

Lab-on-a-chip techniques, which miniaturize various functions and processes at the micro- and nano-scale, benefit from a system transporting macromolecular materials at nanometer length scale. In cells, efficient cytoplasmic transport is achieved by active transport systems in which motor proteins carry cargo along cytoskeletal filaments. The molecular motors convert chemical energy into mechanical work, harnessed by the hydrolysis of adenosine triphosphate (ATP), thereby propelling proteins' along cytoplasmic systems of fibers. An important example is kinesin,[1] a well known, naturally occurring, ubiquitous motor protein which carries cell organelles and macromolecules over considerable distances along microtubule (MT), filaments polymerized from α- and β-tubulin with a diameter of $\sim$25 nm and tens of micrometers in length.[2] These properties of kinesin-based transport are suitable in size for lab-on-a-chip devices composed of a subset of nanoelectromechanical systems (NEMS).

The kinesin heavy chain (KHC), the conventional kinesin component responsible for force generation and hence motility, is constituted of a twin N-terminal catalytic motor domain (head), a dimeric coiled domain (stalk), and a globular C-terminal tail. The KHC enables individual kinesin to move processively towards the (+)-terminus of MTs (anterograde transport) by a highly coordinated alternating head mechanism, taking one 8-nm step for each ATP molecule it hydrolyzes.[3] Upon microtubule binding, a single kinesin molecule can step along MTs for distances up to 1 μm at velocities up to 700 nm/s before detaching from it.

Interest in MTs and its complimentary kinesin motor stems not only from their biological importance (microtubule impairment was suggested as an explanation for the pathogenesis of the Alzheimer's disease,[4] while human pathogens were found to be transported along host cells on kinesin molecules[5]) but are expected as promising tools in the development of synthetic nano-machines. Inspired by such systems it is possible to develop NEMS capable of nanoscale transport by manipulating both the kinesin motor and the cytoskeletal framework. Recent efforts to engineer tailor-made artificial nanotransport systems in order to carry out directional transport of nano-objects in a cell-free environment are thus hardly surprising; kinesin motors have, in fact, been applied for several applications such as biomedical sensors,[6] DNA,[7] and nanoparticle transport.[8] While these methods utilized kinesin and MTs to develop NEMS, they lack in quantitatively evaluating specific interactions between individual molecular shuttle components, most notably, the microtubule-kinesin interaction.

Here, we attempt a real-time kinetic analysis of the microtubule-kinesin interaction using surface plasmon resonance (SPR). SPR has been extensively used in recent years to quantitatively make a kinetic analysis of the dynamic interaction of a mobile biomolecule to a binding partner immobilized onto a specific sensor surface.[9–11] In this approach, there is no need to label both binding partners and binding and dissociation events can be quantitatively monitored in real-time; hence, the binding of kinesins onto MTs can be quantitatively monitored in the same solution in cells and in lab-on-a-chip devices. However, the large molecular weight

a)Author to whom correspondence should be addressed. Electronic mail: teizer@tamu.edu.

of MTs and heterogeneity of its length complicate the SPR study of the microtubule-kinesin interaction.

Here, we report kinetic parameters of adsorption between microtubules and the kinesin motor protein, more specifically; we use the SPR technique under the same conditions as those employed in the development of lab-on-a-chip devices to determine the kinetic parameters between recombinant biotinylated *Drosophila melanogaster* and MTs. The real-time monitoring of the MT-kinesin clearly and quantitatively showed the behavior of kinesin on MT in the presence of ATP, especially, SPR described the smooth dissociation of kinesin by ATP. Further, we also monitored stepwise stacking of nanoparticles on MTs via kinesin-MT and biotin-avidin interactions. We show the potential of the SPR approach for quantitative and real-time analysis for the MT-kinesin interaction.

II. EXPERIMENTAL PROCEDURES

A. Chemicals

Lyophilized porcine brain tubulin was purchased from cytoskeleton. guanosine-5-[(α,β)-methyleno]triphosphate (GMPCPP) to promote microtubule polymerization was purchased from Jena Biosciences. Ethylene glycol bis(2-aminoethylether)-*N*,*N*,*N*′,*N*′-tetraacetic acid (EGTA), piperazine-*N*,*N*′′-bis(2-ethanesulfonic acid) (PIPES), magnesium chloride (1 M), glycerol, paclitaxel (taxol), polysorbate 20 (Tween 20), adenosine 5′-triphosphate *magnesium* salt (MgATP), and adenosine 5′-(β,γ-imido)triphosphate tetralithium salt (AMP-PNP) were purchased from Sigma-Aldrich. 10 mM glycine-HCl (pH 1.5), NaOH (50 mM), 1-ethyl-3-(3-dimethylpropyl)-carbodiimide (EDC), N-hydroxysuccinimide (NHS), and ethanalomine were purchased from BIAcore. Streptavidin-coated quantum dots (QDs) were purchased from Invitrogen and used as received.

B. Microtubule preparation

Porcine tubulin protein was prepared to a final concentration of 50 μM in BRB80 buffer (80 mM PIPES, 1 mM EGTA, 1 mM $MgCl_2$, pH 6.9) containing 1 μM GMPCPP and 5% glycerol, aliquoted and stored at −80 °C. A fresh tubulin aliquot was thawed at 37 °C and allowed to polymerize for 30 min, followed by dilution to 0.5 μM with warm BRB80 buffer supplemented with 20 μM taxol.

C. Kinesin motors preparation

The *D. melanogaster* DNA fragment encoding the full-length kinesin heavy-chain motor domain with the sequences of biotin acceptor peptide (AviTag; GGLNDIFEAQKIEWH) and poly-histidine tag (HHHHHH) in this order at the C-terminus was inserted in the pRA2 expression vector[12] using the NcoI-SacII digestion to produce the plasmids for the recombinant kinesin protein with AviTag at the C-terminus (pRA2b-biokinesin).

We first transformed *Escherichia* (*E.*) *coli* BL21 (DE3) by the plasmid of pBIRAcm encoding biotin ligase (Avidity Inc., Aurora, CO) and then transformed the same cells by the plasmids of pRA2b-biokinesin. The transformed *E. coli* cells were incubated in 2 × YT medium containing 100 g/ml ampicillin and 34 g/ml chloramphenicol at 28 °C. Kinesin and biotin ligase were induced by adding 1 mM isopropylthiogalactoside in the presence of 50 μM of D-biotin (Sigma, St. Louis, MO) and the incubation temperature was decreased to 20 °C. The harvested cells were centrifuged, and the pellet was suspended in a Tris-HCl solution (50 mM, pH 8.0) with 200 mM NaCl, MgATP, and 5 mM mercaptoethanol. After sonication, the suspension was centrifuged at 6300 × g for 30 min, and the supernatant was purified by means of a metal–chelate chromatography column and gel filtration chromatography (Hi-Load 16/60 Superdex 75 size exclusion column, GE Healthcare, Little Chalfont, UK).

Sodium dodecyl sulfate-polyacrylamide gel electrophoresis (SDS-PAGE) and western blotting (using labeled anti-C-term hexa-histidine antibody for fluorescence detection) were carried out to confirm the purity of the expressed protein. The expressed kinesin protein consists of 401 amino acids resulting in a molecular weight of 96 000 Da (dimeric kinesin). Kinesin activity was determined to be 3260 nmol of Pi/min/mg of recombinant kinesin by measuring the rate of ATP hydrolysis using the enzyme linked inorganic phosphate assay (ELIPA) kit from cytoskeleton. Protein concentration was measured by the Bradford Method[13] using the Thermo Scientific Pierce Coomassie Plus Protein Assay, and is expressed as dimer concentrations.

D. Surface plasmon resonance measurement

Binding events of kinesin to microtubules were monitored in real-time using a BIAcore 2000 instrument (BIAcore). All experiments were performed at 25 °C using a running solution of BRB80 supplemented with 0.005% Tween 20 and 100 μM of either MgATP or AMP-PNP at a flow rate of 10 μl/min. Three different sensor chips were used as part of this study, namely, sensor chips CM5, CM3, and C1. Depending on the experiment, either polymerized tubulin (0.5 μM) or kinesin, both in BRB80 buffer, was covalently coupled onto the second channel of the sensor chip by carbodiimide coupling to amine groups using NHS/EDC. Following immobilization, ethanolamine was injected over the sensor's surface in order to deactivate excessive reactive groups. The sensor chip's first channel was used for reference and thus treated similarly to the second channel except that no protein (polymerized tubulin or kinesin) was immobilized on its surface. Lastly, either kinesin (at various concentrations) was injected over immobilized MTs, or microtubules were injected over immobilized kinesin and control surfaces to test for binding. Following SPR sensorgram acquisition, data were normalized by subtracting the response from the reference channel. The kinetic parameters of the microtubule/kinesin complexes were calculated using the BIAevaluation software (BIAcore) global fitting analysis under the assumptions of the 1:1 Langmuir binding model.[14,15]

III. RESULTS

A. SPR approaches for the behavior of MTs on kinesin-immobilized surfaces

In order to analyze the MT-kinesin interaction, kinesins were, first, immobilized on the sensor chips with differently

modified surface (CM5, CM3, and C1). CM5 and CM3 surfaces have a carboxymethyl dextran matrix with one carboxyl group, a thin surface layer with thickness of about 100 nm (CM5) and 30 nm (CM3) in buffer solution per glucose unit, and C1 chip bears a flat carboxylated surface instead of the dextran matrix on CM5 and CM3.

Figures 1(a), 1(c), and 1(e) show the SPR sensorgrams for immobilization of kinesin motors on CM5, CM3 and C1 surfaces, respectively. When 0.5 μM kinesin was applied on each sensor chips after EDC/NHS activation, kinesins were immobilized onto the dextran layers resulting on response levels of 1250 RUs on CM5, 400 RUs on CM3, and less than 40 RUs on C1. The difference of the immobilization capacity on each sensor chip directly influenced the amount of immobilized kinesins. Following kinesin immobilization via NHS and EDC activation, taxol-stabilized microtubules (0.5 μM) in BRB80 buffer supplemented with 100 μM ATP, previously polymerized from 50 μM tubulin, were applied onto the surface to monitor the binding interaction between kinesin and MTs (Figures 1(b), 1(d), and 1(f) for sensor chip CM5, CM3, and C1, respectively. Subtracting the reference channel eliminated all the background contributions). The binding of MTs on immobilized kinesins was observed for all the chips; however, all the measurements yielded low response levels of binding.

B. SPR approaches for the behavior of kinesin proteins on MT-immobilized surfaces

As an alternative condition, we reversed the kinesin/MTs geometry by fixating microtubules and flowing kinesin molecules over it. The flow of kinesin motors over microtubules mimics the natural cell's intracellular transport mechanism, where kinesin motors step along microtubules tracks. Figures 2(a), 1(c), and 1(e) show the immobilization step for 0.5 μM microtubules at the CM5, CM3, and C1 surfaces, respectively. In these cases, MTs were immobilized at the concentration of approximately 300 RUs on CM5, 400 RUs on CM3, and 2300 RUs on C1, indicating that the flat surface of chip was critical to the immobilization of MTs. Following MTs immobilization, kinesin motors (0.5 μM) in BRB80 buffer supplemented with 100 μM ATP were applied into the surface and the binding interaction between kinesin and microtubules was monitored, as shown in Figures 2(b), 2(d), and 2(f) for sensor chip CM5, CM3, and C1, respectively. Subtracting the reference channel eliminated all background contributions.

As seen in Figure 2(f), the C1 sensor chip offers a better environment for kinesin/microtubule complexes binding analysis compared to the CM5 (Fig. 2(b)) and CM3 (Fig. 2(d)) sensors. This result implies that the flat surface of C1 led to appropriate immobilization of MTs in amount and structure for kinesin to bind onto immobilized MTs. It is clear that conditions used when obtaining the sensorgrams displayed in Figure 2 are more meaningful than those employed in Figure 1. The reason for this will be outlined in the discussion below.

C. Quantitative SPR analysis of the interaction between kinesins and microtubules

As a result of the stable measurement of the MT-kinesin interactions by immobilization of MTs on the C1 sensor

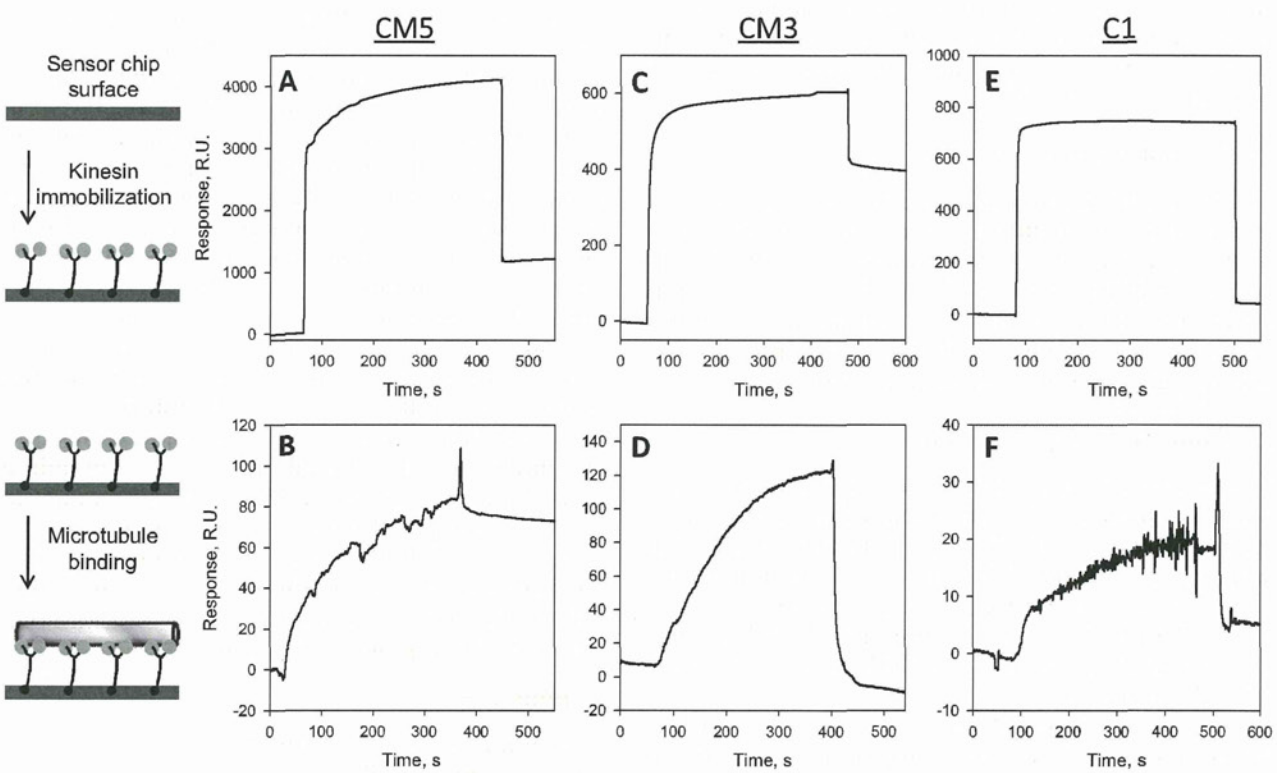

FIG. 1. Real-time SPR sensorgrams for the immobilization of kinesin protein on CM5 (a), CM3 (c), and C1 (e) sensor surfaces; and sensorgrams showing microtubule binding interactions with kinesin-coated CM5 (b), CM3 (d), and C1 (f) sensor chips. For clarity reasons, all figures are displayed as differential sensorgrams, after subtraction from the reference channel.

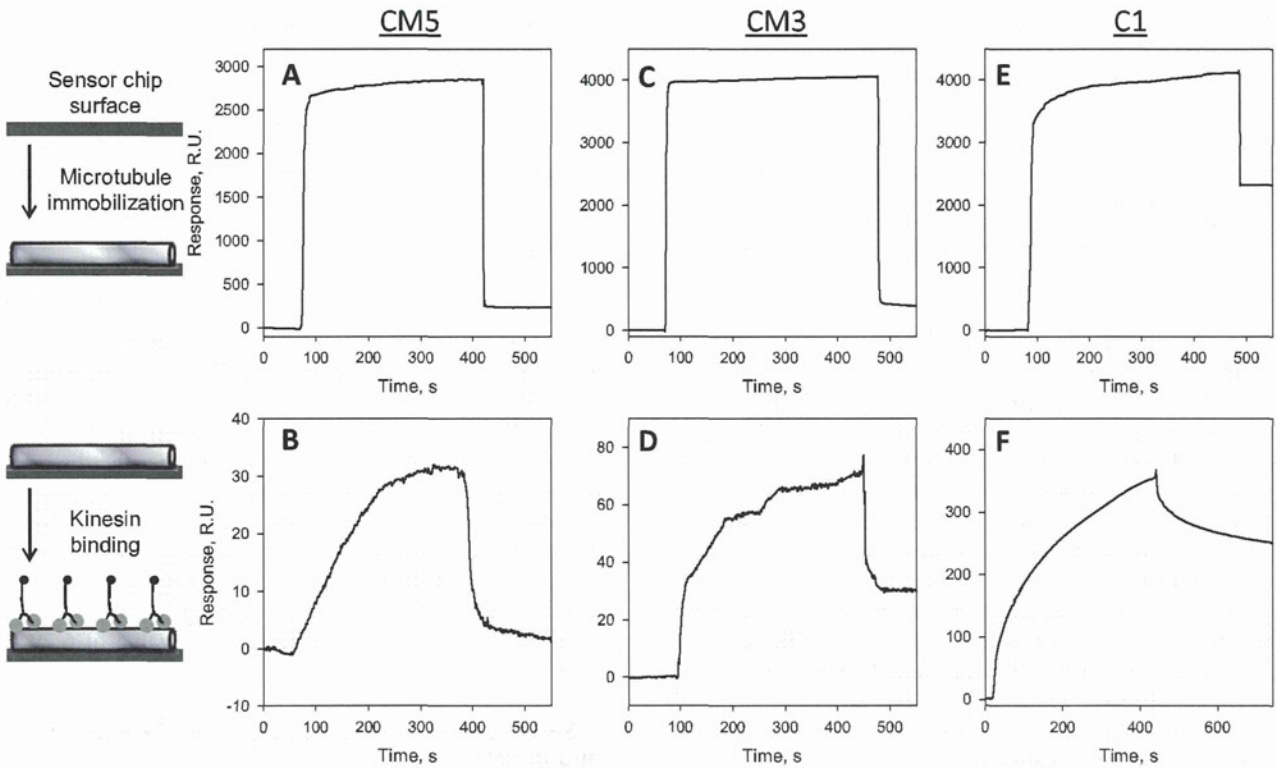

FIG. 2. Real-time SPR sensorgrams for the immobilization of 0.5 μM taxol-stabilized microtubules on CM5 (a), CM3 (c), and C1 (e) sensor surfaces; and sensorgrams showing kinesin binding interactions with microtubule-coated CM5 (b), CM3 (d), and C1 (f) sensor chips. For clarity reasons, all figures are displayed as differential sensorgrams, after subtraction from the reference channel.

chip, we made a quantitative analysis to determine the kinetic parameters of MT-kinesin interaction in the ATP-containing solution where kinesin motors are applied over bound MTs. Both affinity and kinetic aspects of the MT-kinesin interaction were determined from obtained sensorgrams, particularly the dissociation and association rates (k_{on} and k_{off}, respectively).

Kinesin at five different concentrations (namely 800, 1000, 1200, 1400, and 1800 nM in BRB80 buffer supplemented with 100 μM ATP) were injected into the C1 surface in order to bind to previously immobilized microtubules. Figure 3 shows the SPR sensorgram of the association and dissociation phases for all five kinesin concentrations to MTs immobilized on the chip after subtracting the reference channel from each SPR sensorgram individually. The on-rate of the kinesin-microtubule interaction is proportional to kinesin's concentration, indicating that it is sufficiently controlled to quantitatively analyze kinetic parameters.

Using both the association and dissociation phase data sets displayed in Fig. 3, association rate constant (k_{on}), dissociation rate constant (k_{off}), and dissociation binding constants (K_d) were determined by globally fitting SPR sensorgrams responses with a 1:1 Langmuir interaction model resulting in the following kinetic parameters: $k_{on} = 2.23$ (± 0.33) $mM^{-1}s^{-1}$; $k_{off} = 0.19$ (± 0.07) $\times 10^{-3}\,s^{-1}$; $K_d = 86.27$ (± 11.85) nM, fitted with an associated χ^2 value of 5.68 ± 2.29 (Table I).

The key to kinesin processivity is its ATPase cycle which is related to the dependence of kinesin-microtubule affinity to nucleotides, that is, a specific cycle of kinesin strong binding to MTs when its nucleotide-binding site is empty or in the presence of ATP and a weak binding state when bound to ADP, leading to detachment from MTs. Consequently, varying the nucleotide bound to kinesin motors will lead to changes on its equilibrium dissociation constants to microtubules. A robust technique intended to determine dissociation constants of constructed kinesin motors molecular nanotransport systems should in turn, be capable of

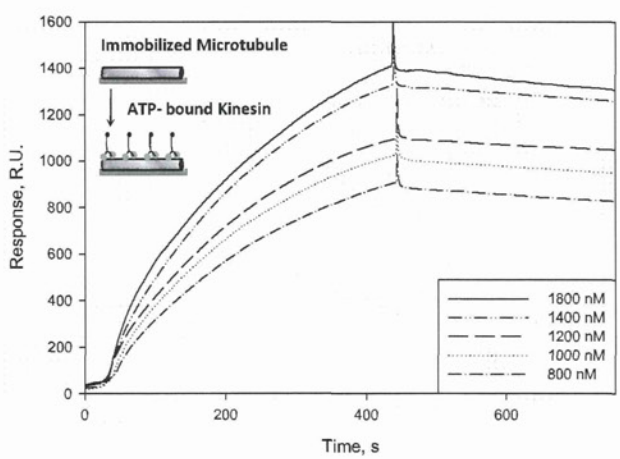

FIG. 3. Kinesin-microtubule interaction monitored by SPR. Kinesin was injected over microtubules immobilized on a C1 sensor chip. Running buffer was BRB80 supplemented with 100 μM MgATP and 0.005% Tween 20 at a flow rate of 10 μl/min.

TABLE I. Kinetic binding parameters of kinesin motor protein with immobilized microtubules using the C1 BIAcore® sensor surfaces.

	Immobilized MT response (R.U.)	Kinesin binding response (R.U)[a]	k_{on} (mM^{-1} s^{-1})[b]	k_{off} (s^{-1})[b]	K_d (nM)[c]
ATP	2377.15	1313.07	2.23 ± 0.33	$0.19\ (\pm 0.07) \times 10^{-3}$	86.27 ± 11.84
AMP-PNP	2374.05	1973.93	2.92 ± 0.71	$8.99\ (\pm 0.87) \times 10^{-6}$	2.64 ± 1.01

[a]Binding response acquired for kinesin protein injected at 1 μM.
[b]Values represent mean rate constants determined by two replicates ($\pm$s.e.m.).
[c]Equilibrium dissociation constant determined by the ratio between k_{on} and k_{off} ($k_d = k_{off}/k_{on}$).

detecting changes in measured K_d values while nucleotide variations are made.

Here, SPR measurement was performed for MT-kinesin interaction in the presence of an ATP nucleotide analog, AMP-PNP, which mimics the ATP binding to the motor protein but is extremely slowly hydrolyzed.[16] Figure 4 illustrates the SPR sensorgrams of the binding and dissociation phases for all five kinesin concentrations to bound MTs after subtracting the reference channel from each SPR sensorgram individually. The average baseline resonance response for the five separate microtubule immobilization was 2374.05 ± 178.28 R.Us. No MTs were bound to the sensor's reference channel, which was used to eliminate any background contributions by subtracting it from each kinesin injected test channel individually.

As observed in Figure 4, kinesin, at concentrations ranging from 800 to 1800 nM, was injected over immobilized microtubules to test the effect of the ATP analog AMP-PNP nucleotide to the binding profiles. Each kinesin concentration was injected in duplicate. Association phase of kinesin binding to the MTs covered surface was monitored during 400 s, yielding curvatures of each binding response, which helps define the kinesin-microtubule complex formation kinetics. At the highest injected kinesin concentration (1800 μM), an approximate 60% increase in relative resonance units is achieved when ATP was substituted with AMP-PNP in the kinesin's reactive site. Such observation was an expected trend, as the ATP analog, being a lesser potent microtubule dissociator than ATP, will tighten the binding of kinesin to MTs, and consequently lowers K_d. This indicates that binding of kinesin to MTs when AMP-PNP is bound to kinesin is significantly greater than the ATP-bound to the motor. Therefore, the dissociation binding constant value was calculated following identical procedures as previously described. The 1:1 Langmuir interaction model was able to properly fit the SPR response data giving the following kinetic parameters: $k_{on} = 2.92\ (\pm 0.71)\ mM^{-1}\ s^{-1}$; $k_{off} = 8.99\ (\pm 0.87) \times 10^{-6}\ s^{-1}$; $K_d = 2.64\ (\pm 1.01)$ nM with a calculated χ^2 value of 6.29 ± 3.31 (Table I).

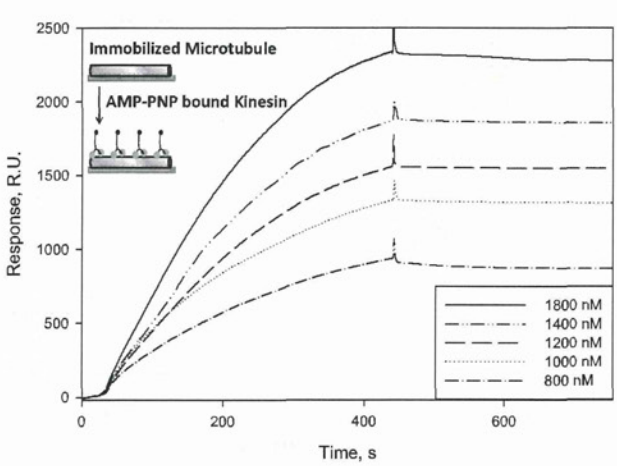

FIG. 4. Kinesin-microtubule interaction monitored by SPR. Kinesin was injected over microtubules immobilized on a C1 sensor chip. Running buffer was BRB80 supplemented with 100 μM AMP-PNP and 0.005% Tween 20 at a flow rate of 10 μl/min.

D. SPR analysis for stepwise stacking of kinesin and nanoparticles on MTs

In order to analyze the affinity for individual components of engineered molecular shuttles in real-time using SPR, the presented method should be able to not only monitor the kinesin/microtubules binding events, but also the kinesin/cargo binding properties. Inspired by nanoparticle transport studies,[17–19] where a specific cargo is bound to recombinant kinesin via its biotin tag, the binding events of kinesin to commercial available streptavidin-coated QDs could be evaluated using the BIAcore technology. Accordingly, Figure 5 shows SPR sensorgrams for the stepwise injection of kinesin and QD to immobilized microtubules onto a C1 sensor surface. After activating carboxylic acid groups on both the first and second sensor's channels with NHS/EDC, microtubules at a concentration of 0.5 μM were injected only over the second channel, leaving the first channel to be used as a negative control channel. Ethanolamine, kinesin (0.5 μM), and QDs (10 nM) were sequentially injected over both channels, and the surface plasmon resonance measured and plotted. Figure 5(a) shows the raw real-time SPR responses for the kinesin and quantum dot injections while Figure 5(b) shows the normalized SPR sensorgram obtained by subtracting the response from the negative control channel (for clarity, only the kinesin and quantum dot injection steps were plotted). To minimize kinesin dissociation from microtubules, injection of the QDs was performed as soon as possible after the start of the kinesin/MTs dissociation process, causing a decrease of approximately 50 RUs on the kinesin response level.

Independently, we could confirm proper assembly of kinesin nanotransport system by the visualization of quantum dots transport through kinesin motion along fluorescently labeled immobilized microtubules by fluorescence microscopy (data not shown).

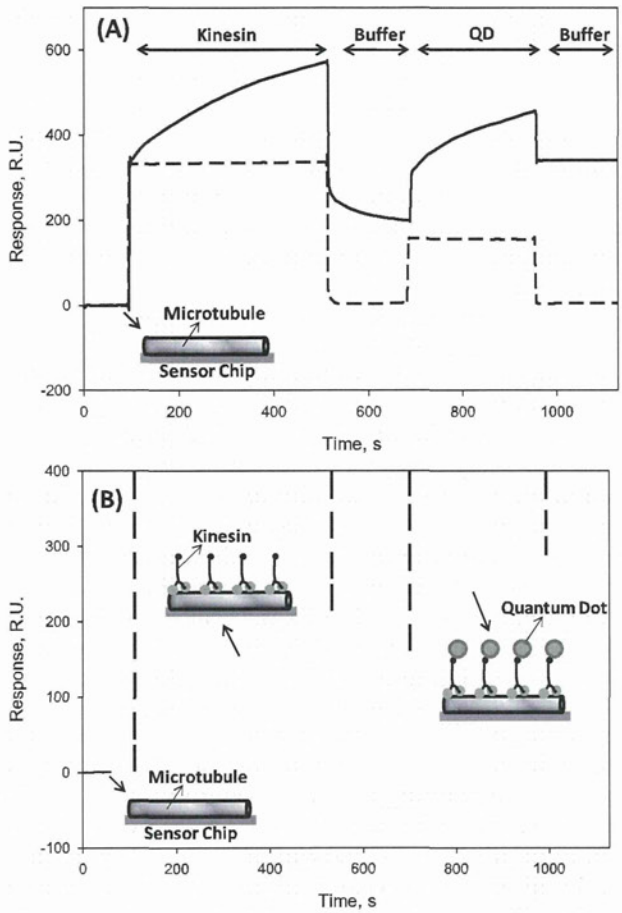

FIG. 5. SPR sensorgrams for the binding behavior of the stepwise immobilization of the kinesin (0.5 μM) and streptavidin-conjugated QD particles (10 nM) on the microtubule-coated surface of a C1 sensor chip. (a) Raw sensorgram showing resonance responses on both working (solid line) and reference (dashed line) channels; and (b) SPR sensorgram plotted after subtraction from the negative control channel.

IV. DISCUSSION

A. Appropriate surface structure on sensor chips for SPR analysis

Microtubule protofilaments prepared at identical conditions as those employed here were shown to have an average length of about 10 μm,[20,21] suggesting that even though kinesin molecules were covalently coupled to the matrix of sensor chips CM5 and CM3, the thickness and geometry of such layers might prevent microtubule filaments from reaching its binding partners, i.e., kinesin. Thus, the limited interactions between MTs and kinesin when using both CM5 and CM3 sensor may be restricted to microtubules interacting with kinesin molecules confined to the brink of the dextran matrix, as indicated by the low response levels seen in Figures 1(b) and 1(d). However, the 30 nm dextran layer on the CM3 sensor provided a better environment for microtubules to come in close contact with immobilized kinesin motors when compared to the 100 nm dextran layer on the CM5 sensor surface, indicating that microtubules can reach a larger number of immobilized kinesin motors when utilizing the shorter dextran layer. Collectively, we conclude that MTs are unable to reach the majority of kinesin molecules that are confined within the dextran surface layer, making the dextran-deficient C1 sensor chip an attractive alternative for such investigation. In spite of that, the flat carboxymethylated surface associated with the C1 sensor chip greatly reduced the kinesin immobilization capacity at the C1 surface to 36 RUs, a striking difference when compared to the immobilization responses of kinesin motors on CM5 and CM3 surfaces, 1250 and 400 RUs, respectively. Furthermore, the lack of the flexible dextran matrix on the C1 sensor surface implies that kinesin motors are not able to freely rotate within the surface layer, which in turn might result in motors not being optimally aligned to interact with microtubules, decreasing possible interactions between microtubules and kinesin. Consequently, the binding of microtubules to the C1 surface was observed with low response levels associated with small signal-to-noise ratios, as seen in Figure 1(f).

Geometric considerations for the sensor's dextran layer as well as microtubule lengths are not the only reason for the low microtubule response binding levels observed on all three sensor surfaces after the immobilization of kinesin to the surface. One must also consider the activity of the surface-bound kinesin. It is well known that without prior surface pretreatment with other proteins (e.g., casein) to block the surface, kinesin can denaturate on the surface and consequently lose its ability to interact with microtubules,[22,23] which would in turn explain the low response levels of microtubule binding to surface-bound kinesin (Figure 1). Additionally, chemically binding the motor protein to the sensor chip surface will not favor proper orientation of the kinesin's motor domain relative to microtubules, and since such orientation is essential for microtubule interaction,[24] the low response level of binding observed in Figure 1 may be a consequence of the chemical immobilization of kinesin.

Even though it is possible to directly visualize the binding of microtubules to surface bound kinesin in Figure 1, especially when using the CM3 sensor surface, the main purpose of such experiment, the determination of the kinesin/MTs equilibrium association (k_{on}) and dissociation (k_{off}) rates constants, and consequently the equilibrium dissociation constant ($K_d = k_{off}/k_{on}$), cannot be achieved using data displayed in Figure 1. This is because K_d values, required for evaluation of the strength and binding rate of the kinesin-MTs nanotransport system, can be readily derived from the sensorgram given previous knowledge of the concentration of the analyte interacting with the fixed ligand,[25] i.e., precise concentration of the analyte is a prerequisite for accurate determination of kinetic parameters. However, the exact microtubule concentration is hard to assess, mainly due the fact that MTs polymerize with rather broad length distributions. Several techniques were tested in order to manipulate the MT size distribution, while they were able to control the sizes of polymerized protofilaments, they could not provide uniform microtubule lengths. For example, shearing and annealing leads to a decrease and increase of the average MT length, respectively; however, both methods were not effective in reducing polydispersity.[26]

Since the kinesin concentration can be precisely determined using the Bradford method, the geometry of assembled molecular shuttles was reversed, i.e., kinesin motors flushed over immobilized MTs, and a comparison between the three employed sensor chips revealed that the C1 sensor is particularly suited for investigation of the kinesin/microtubule complexes binding analysis (Figure 2(f)). The dextran matrix on both CM3 and CM5 sensors might hinder access of microtubules to activated amine-reactive sulfo-NHS esters within the dextran layer, resulting in poor fixation of MTs whose immobilization may be limited to activated sites located at the brink of the layer. In contrast, the high immobilization level of microtubules on the C1 surface lead to expressive binding events of injected kinesin motors, indicating that the absence of a dextran layer is favorable for binding studies of bulky biomolecule ligands, which can be better immobilized onto the sensor surface.

B. Kinetic parameters calculated from SPR sensorgrams

Table I summarizes kinetic and equilibrium results obtained using the C1 sensor surface when the ATP and the ATP analog AMP-PNP was bound to kinesin motors.

Using the C1 surface, kinetic parameters of kinesin/microtubule binding events could be elucidated under conditions similar to those used by researchers when analyzing the cargo transport of kinesin molecular shuttles by fluorescent microscopy.[8,27,28] Table I summarizes kinetic and equilibrium data obtained using the C1 sensor surface when the ATP and the ATP analog AMP-PNP was bound to kinesin motors.

Kinetic data calculated when the ATP nucleotide was bound to kinesin suggest that kinesin/microtubule binding is tight. Reported dissociation constant values usually range from 37 nM to approximately 100 nM;[29,30] however, values as high as 12.39 μM are also found in the literature.[31] Direct comparison between reported K_d values is not straightforward as expressed kinesins are usually expressed under different conditions and with different tags, which influence affinity between said protein and a given analyte. Moreover, each group uses theirs specific technique for the constant determination, which also leads to discrete data interpretation methods. The slightly higher value for kinesin-microtubules dissociation constant reported here, indicating looser kinesin-microtubule complex formation in the presence of ATP, might be due to the global fit model chosen. Obtained SPR sensorgrams (Figure 3) were also fitted using different models, a total of three models were used to test the robustness of the SPR technique in determining this specific interaction. The 1:1 Langmuir interaction model provided the best fit of the data ($\chi^2 = 5.68$), while both the heterogeneous analytes and the heterogeneous ligand models resulted in poor fitting, indicated by the relatively high χ^2 values, 126 and 42, respectively.

Regarding association and dissociation rates, Gilbert and coworkers performed the most thorough kinetic studies of kinesin. With the aid of the stopped-flow technique, they reported k_{on} and k_{off} values for the kinesin/microtubule complex by monitoring turbidity changes as a function of time when kinesin and microtubule solutions were rapidly mixed.[29,32,33] Thus, even though kinetic parameters have already been widely reported in the literature, conditions on which the kinesin/microtubule interactions were studied are strikingly distinct from the conditions employed here. More importantly, the k_{on} and k_{off} values are reported at conditions identical to those where kinesin-based synthetic nanotransport systems are assembled, namely, where kinesin and microtubules interact in a nucleotide-rich environment (i.e., ATP) over several minutes.

Considering k_{on} determination, values reported by Gilbert and coworkers fall within 10 and 20 $\mu M^{-1} s^{-1}$,[29,33] however, such values correspond to the pre-steady-state kinetics of kinesin/MTs association, where changes in turbidity were monitored for a total of 500 ms. That is a striking deviation from our study where the association kinetics was determined by monitoring the kinesin/microtubule interaction over several minutes. Also, stopped-flow experiments were performed by mixing solutions of microtubules to kinesin at buffers with no supplemented nucleotide, i.e., no ATP or AMP-PNP was bound to kinesin as it complexes with microtubules. Since the kinesin/MTs interaction is nucleotide dependent, the discrepancy between k_{on} values reported by Gilbert *et al.* and our group are expected, which can be seen by our calculated k_{on} value of $2.23 \pm 0.33\ mM^{-1} s^{-1}$. The larger association rate constant reported here is therefore due to the fact that the SPR technique measures the level of binding between kinesin and microtubules at the steady state, to the extent where dissociated kinesin is allowed to "re-bind" to the microtubule-covered sensor surface, in contrast to the stopped-flow method where reported k_{on} values are pre-steady state.

As for the dissociation rate constants, k_{off} values reported by Gilbert *et al.* were ATP-promoted, that is, turbidity changes were measured after ATP was added to the kinesin/MT mixture, which promoted the complex dissociation. Therefore, reported k_{off} values include the kinesin-ATP association step, resulting in the slower dissociation rates.

When the ATP nucleotide was replaced by its nonhydrolysable analog AMP-PNP, SPR data demonstrated that the binding of kinesin to MTs became substantially stronger, as indicated by a decrease of over 90% in the equilibrium dissociation constant. The K_d value reported here, i.e., 2.64 ± 1.01 nM, is considerably lower than the value reported by others, namely, 0.27 ($\pm$ 0.15) μM;[31] however, the latter K_d value was obtained when 1 mM AMP-PNP was bound to kinesin, which will undoubtedly change the conformation of the motor protein and thus its equilibrium dissociation constants. Moreover, such disagreement is also a consequence of the same factors as previously discussed, i.e., a combination of different techniques followed by separate data fitting protocols and here, the forceful fitting of the kinesin-microtubule interaction to a simple 1:1 interaction model. Unfortunately, we could not find any kinetic studies, which showed k_{on} and k_{off} calculations when AMP-PNP was bound to kinesin. It should be noted that there is no noticeable distinction between the obtained k_{on} when AMP-PNP was bound to kinesin instead of the ATP nucleotide, indicating a comparable rate of kinesin/MT association. In contrast,

calculated k_{off} values are substantially different between the two nucleotides. The slower rate of kinesin dissociation from microtubules when AMP-PNP is bound to the motor protein seems to be a consequence of the stronger kinesin/MT binding events, slowing down the release of kinesin from microtubules. Kinesin-microtubule kinetic parameters as well as immobilization intensities obtained with the aid of the SPR technique are summarized in Table I.

Although it is over simplistic to assume that interactions between MTs and kinesin motors follows a simple 1:1 interaction model, which is equivalent to the Langmuir isotherm for adsorption to a surface, the data could be fitted well by such model. It was previously reported by others that the kinesin heavy-chain domain binds to MTs with an axial repeat of 8 nm and a stoichiometry of one kinesin motor molecule per tubulin heterodimer,[34] making the microtubule protofilaments capable of multiple interactions with kinesin motors.

To better comprehend individual interactions of each component of kinesin nanotransport systems, the interaction between kinesin motors and a given cargo was investigated through the SPR technique relying on the expressed protein's biotin tag. Stepwise stacking of kinesin motors and streptavidin-coated quantum dots (~20 nm diameters) on C1 microtubule-coated surfaces is seen in Figure 5(b). It is clear from the figure that the SPR method can be employed for monitoring the assembly of kinesin-based nanoscopic machines; multi-stacking binding events of microtubule-kinesin, and kinesin-quantum dots could be visualized in real time. Little removal of the immobilized kinesin/QD conjugate was observed while BRB80 buffer was flushed into the system, which is a consequence of the strong interaction between biotin and streptavidin, resulting in very slow dissociation rates (step 5). In addition, it is evident from Figure 5(a) that there are no non-specific binding events of either kinesin or quantum dots to the microtubule-coated surface, as no SPR response was observed on the reference channel (dashed line in Figure 5(a)).

V. CONCLUSIONS

In summary, it has been demonstrated that the surface plasmon resonance (SPR) technique is particularly suited for the monitoring of interactions between individual components of molecular shuttles, namely, microtubule-kinesin-cargo. Results from the SPR study show that the method can be used in the determination of kinetic parameters between kinesin motors and microtubules at similar conditions routinely used by several researchers when designing biotinylated kinesin nanotransport systems. It was found that the BIAcore C1 sensor chip could be used for the immobilization of polymerized microtubules, whereas the CM-class chips are unable to properly immobilize microtubules, which may be a consequence of long dextran layers present on the latter surfaces. Furthermore, injection of kinesin over bound microtubule protofilaments, in the presence of both ATP and its non-hydrolysable analog AMP-PNP, resulted in consistent binding profiles that could in turn be used to determine the effective kinetic parameters. Moreover, it was clearly demonstrated that the stepwise stacking of kinesin and quantum dots cargo on a microtubule-coated surface could be evaluated in real-time using the method reported here.

ACKNOWLEDGMENTS

This work was supported by the WPI Program of the Japan Society for the Promotion of Science (JSPS). We acknowledge helpful communication with Dr. Wonmuk Hwang and Dr. John Noel.

[1]R. D. Vale, and R. A. Milligan, Science **288**, 88 (2000).
[2]T. Kreis and R. D. Vale, *Guidebook to the Cytoskeletal and Motor Proteins* (Oxford University Press, Oxford, UK, 1993), pp. 189–196.
[3]M. J. Schnitzer and S. M. Block, Nature **388**, 386 (1997).
[4]A. C. Alonso, I. Grundke-Iqbal, and K. Iqbal, Nat. Med. **2**, 783 (1996).
[5]J. Rietdorf, A. Ploubidou, I. Reckmann, A. Holmstrom, F. Frischknecht, M. Zettl, T. Zimmermann, and M. Way, Nature Cell Biol. **3**, 992 (2001).
[6]G. D. Bachand, S. B. Rivera, A. Carroll-Portillo, H. Hess, and M. Bachand, Small **2**, 381 (2006).
[7]S. Diez, C. Reuther, C. Dinu, R. Seidel, M. Mertig, W. Pompe, and J. Howard, Nano Lett. **3**, 1251 (2003).
[8]R. K. Doot, H. Hess, and V. Vogel, Soft Matter **3**, 349 (2007).
[9]T. Ibii, M. Kaieda, S. Hatakeyama, H. Shiotsuka, H. Watanabe, M. Umetsu, I. Kumagai, and T. Imamura, Anal. Chem. **82**, 4229 (2010).
[10]H. Watanabe, T. Nakanishi, M. Umetsu, and I. Kumagai, J. Biol. Chem. **283**, 36031 (2008).
[11]M. Umetsu, T. Hattori, S. Kikuchi, I. Muto, T. Nakanishi, H. Watanabe, and I. Kumagai, J. Mater Res. **23**, 3241 (2008).
[12]I. Makabe, R. Asano, T. Ito, K. Tsumoto, T. Kudo, and I. Kumagai, Biochem. Biophys. Res. Commun. **328**, 98 (2005).
[13]M. M. Bradford, Anal. Biochem. **72**, 248 (1976).
[14]I. Langmuir, J. Am. Chem. Soc. **40**, 1361 (1918).
[15]Biacore, *BIAevaluation 4.0 Software Handbook* (Biacore AB, Uppsala, Sweden, 2004).
[16]S. T. Brady, Nature **317**, 73 (1985).
[17]G. Muthukrishnan, B. M. Hutchins, M. E. Williams, and W. O. Hancock, Small **2**, 626 (2006).
[18]A. Seitz, and T. Surrey, EMBO J. **25**, 267 (2006).
[19]E. D. Spoerke, G. D. Bachand, J. Liu, D. Sasaki, and B. C. Bunker, Langmuir **24**, 7039 (2008).
[20]J. Noel, W. Teizer, and W. Hwang, ACS Nano **3**, 1938 (2009).
[21]J. Noel, W. Teizer, and W. Hwang, J. Visualized Exp. **30**, 30 (2009).
[22]J. Howard, A. J. Hudspeth, and R. D. Vale, Nature **342**, 154 (1989).
[23]V. Verma, W. O. Hancock, and J. M. Catchmark, J. Biol. Eng. **2**, 14 (2008).
[24]D. S. Martin, R. Fathi, T. J. Mitchison, and J. Gelles, Proc. Natl. Acad. Sci. **107**, 5453 (2010).
[25]L. Tirian, E. Hlavanda, J. Olah, I. Horvath, F. Orosz, B. Szabo, J. Kovacs, J. Szabad, and J. Ovadi, Proc. Natl. Acad. Sci. **100**, 13976 (2003).
[26]Y. Jeune-Smith and H. Hess, Soft Matter **6**, 1778 (2010).
[27]G. D. Bachand, S. B. Rivera, A. K. Boal, J. Gaudioso, J. Liu, and B. C. Bunker, Nano Lett. **4**, 817 (2004).
[28]A. Carroll-Portillo, M. Bachand, A. C. Greene, and G. D. Bachand, Small **5**, 1835 (2009).
[29]L. M. Klumpp, A. T. Mackey, C. M. Farrell, J. M. Rosenberg, and S. P. Gilbert, J. Biol. Chem. **278**, 39059 (2003).
[30]G. Woehlke, A. K. Ruby, C. L. Hart, B. Ly, N. Hom-Booher, and R. D. Vale, Cell **90**, 207 (1997).
[31]I.-M. T. C. Crevel, A. Lockhart, and R. A. Cross, J. Mol. Biol. **257**, 66 (1996).
[32]S. P. Gilbert, M. R. Webb, M. Brune, and K. A. Johnson, Nature **373**, 671 (1995).
[33]C. M. Farrell, A. T. Mackey, L. M. Klumpp, and S. P. Gilbert, J. Biol. Chem. **277**, 17079 (2002).
[34]B. C. Harrison, S. P. Marchese-Ragona, S. P. Gilbert, N. Cheng, A. C. Steven, and K. A. Johnson, Nature **362**, 73 (1993).

Bioconjugate Chemistry

Article

pubs.acs.org/bc

A High-Affinity Gold-Binding Camel Antibody: Antibody Engineering for One-Pot Functionalization of Gold Nanoparticles as Biointerface Molecules

Takamitsu Hattori,[†] Mitsuo Umetsu,*[,†,‡] Takeshi Nakanishi,[†] Satoko Sawai,[†] Shinsuke Kikuchi,[†] Ryutaro Asano,[†] and Izumi Kumagai*[,†]

[†]Department of Biomolecular Engineering, Graduate School of Engineering, Tohoku University, Aoba 6-6-11, Aramaki, Aoba-ku, Sendai 980-8579, Japan

[‡]Center for Interdisciplinary Research, Tohoku University, Sendai, Aoba 6-3, Aramaki, Aoba-ku, Sendai 980-8578, Japan

Supporting Information

ABSTRACT: Antibodies, with their high affinity and specificity, are widely utilized in the field of protein engineering, medicinal chemistry, and nanotechnology applications, and our recent studies have demonstrated the recognition and binding of antibody for the surface on inorganic material. In this study, we generated a high-affinity gold-binding antibody fragment by a combination of peptide-grafting and phage-display techniques and showed the availability of the material-binding fragment for one-pot functionalization of nanoparticles as interface molecules. After a gold-binding peptide sequence was grafted into one of the complementarity determining regions of a single variable domain of a heavy-chain camel antibody, a combinatorial library approach raised by 20 times the affinity of the peptide-grafted fragment. The high-affinity gold-binding fragment (E32) spontaneously adsorbed on gold nanoparticles, and consequently the nanoparticles formed a stable dispersion in a high-ionic-strength solution. Multivalent and bispecific antibodies constructed on the E32 platform by means of fusion technology functionalized gold nanoparticles in one pot, and these functionalized nanoparticles could be used to obtain surface plasmon resonance scattering images of cancer cells and to spontaneously link two different nanomaterials. Here, we propose the bispecific antibodies as convenient interface molecules in the nanosized world.

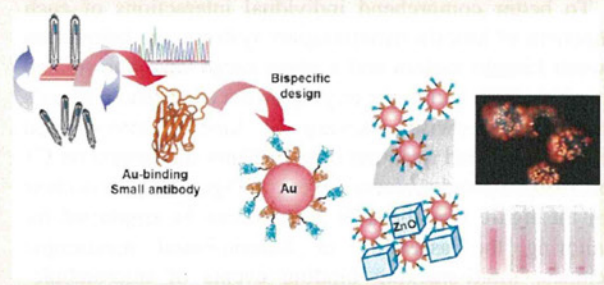

INTRODUCTION

The downsizing of inorganic materials can impart unique electrical, photonic, and optical properties to the materials. Inorganic nanomaterials have been used as probes for biological sensing and imaging,[1,2] and they can also serve as building blocks in bottom-up construction of nanodevices.[3,4] For example, semiconductor nanomaterials called quantum dots exhibit size-dependent fluorescence and are widely used for cellular imaging,[5] and superparamagnetic iron oxide particles have been used for signal amplification in magnetic resonance imaging.[6] Homogeneous inorganic nanocrystals with defined shape and surface characteristics self-assemble into square and hexagonal packing,[7] and two types of nanoparticles with different sizes and shapes have been shown to assemble into a binary superlattice.[8] For both biological and nanotechnological applications, nanoparticles must form stable dispersions in solution and have surfaces designed to interact with targets such as proteins, cells, or nanoparticles. However, the methods for preparing nanoparticles with these two characteristics vary widely depending on the materials, and thus a trial and error process is required.

One method for preparing nanoparticles with the desired properties involves the use of material-binding peptides. During the past decade, several peptides with affinity for nonbiological materials, such as metals, metal oxides, and semiconductors, have been identified by means of combinatorial library approaches.[9,10] Such material-binding peptides have been used for bottom-up fabrication of bionanotechnology applications, such as patterning and assembly of proteins and nanomaterials,[11−13] biofunctionalization of nanoparticles,[14,15] and synthesis of crystalline metal nanoparticles.[16−18] However, the binding affinities of peptides are often not high enough for such applications.[19,20] Recently, we focused on antibodies as alternative material-binding molecules because they have higher affinities and specificities than peptides.[21,22] We prepared several antibody fragments with high affinity for the surface of inorganic nanomaterials;[20,23,24] the fragments strongly bind to the surface of specific inorganic nanoparticles, and the resulting

Received: June 15, 2012
Revised: August 5, 2012
Published: August 8, 2012

dx.doi.org/10.1021/bc300316p | *Bioconjugate Chem.* 2012, 23, 1934−1944

nanoparticles can be as stably dispersed as proteins, even in high-salt buffer.[24]

In this study, we demonstrate the potential of material-binding antibodies as interface molecules that can stably disperse nanoparticles in high-ionic-strength solutions and simultaneously bind to targets. Gold nanomaterials are among the most well-studied nanomaterials. Gold nanostructures scatter and absorb visible and near-infrared light at a plasmon resonance wavelength that depends on the size and shape of the structure, and these characteristics have been used for biosensing,[25] imaging,[26] and optical nanocircuitry.[27] Here, we generated antibody fragments with high affinity and specificity for gold surfaces by means of a method we refer to as the "construction of antibodies by integrating grafting and evolution technology" (CAnIGET, Scheme 1),[20] in which the single variable domain of the heavy chain of a heavy chain camel antibody (VHH fragment) was functionalized by a combination of peptide grafting and in vitro selection. The generated high-affinity gold-binding VHH fragment (designated E32) strongly adsorbed on gold nanoparticles, which could then be stably dispersed in a high-ionic-strength solution. In addition, we designed and constructed two bispecific antibodies by joining two different VHH fragments. A bispecific antibody comprising a VHH fragment with affinity for gold nanoparticles and a VHH fragment with affinity for the epidermal growth factor receptor (EGFR) on cancer cells enabled us to obtain surface plasmon resonance (SPR) scattering images of the cells; and a bispecific antibody constructed from gold-binding and ZnO-binding VHH fragments allowed us to spontaneously link two different nanomaterials. Here, we propose a new methodology for stable dispersion of nanoparticles together with functionalization in one pot by using high-affinity material-binding antibody fragments.

Scheme 1. Construction of High-Affinity Material-Binding Antibody Fragments and Multivalent and Bispecific Antibody Fragments

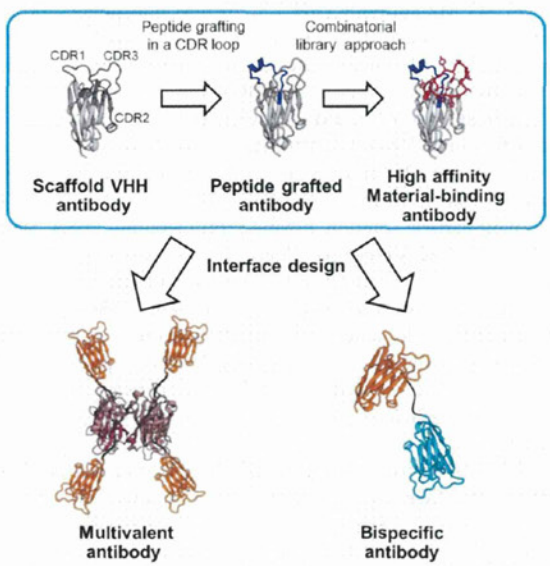

EXPERIMENTAL PROCEDURES

Construction of the Expression Vector for VHH Fragments with a Gold-Binding Peptide in Complementarity Determining Regions (CDRs). The DNA sequence coding VHH_{GBP1}, a VHH fragment with a previously reported gold-binding peptide (GBP: LKAHLPPSRLPS)[28] in the CDR 1 loop, was synthesized by means of overlap extension PCR from a pRA-wtVHH-FLAG plasmid.[20] The gene fragments were inserted into *Nco*I–*Sac*II restriction sites of pRA-FLAG vectors to produce the pRA-VHH_{GBP1}-FLAG plasmid.

Construction of a Phage Library and Selection of VHH Fragments with High Affinity for Gold Surfaces. Construction of phage library and selection of VHH fragments with high affinity for gold surfaces were performed by means of the CAnIGET method.[20] Briefly, a gene encoding the VHH_{GBP1} fragment with a randomized sequence in the CDR3 loop was amplified from the pRA-VHH_{GBP1}-FLAG plasmid and inserted into the phagemid vector pTZ-PsFv2.[29] For the selection of VHH fragments with high affinity for gold surfaces, approximately 10^9 phages were mixed with 1 mg of gold powder (particle size <10 μm, Sigma-Aldrich, Tokyo, Japan) in a 10 mM phosphate solution (pH 7.5) containing 200 mM NaCl and 0.05% Tween 20. After the powder was washed with the phosphate solution five times, residual phages bound to the gold surface were eluted with 500 mM phosphate solution (pH 7.5) containing 200 mM NaCl. This panning procedure was performed four times, during which the phosphate concentration of the washing solution was increased from 30 to 50 mM (second wash, 30 mM; third and fourth washes, 50 mM). The amino acid sequences of 100 randomly chosen clones were analyzed. The selected VHH genes were inserted into the *Nco*I–*Sac*II restriction sites in the pRA-FLAG vector for expression in *Escherichia* (E.) *coli*.

Construction of Expression Vectors for Biotinylated VHH and Bispecific VHH Dimers. To construct bispecific antibodies with affinity for gold and EGFR, and with affinity for gold and ZnO, the gene for E32 VHH was fused at the C-terminus of Ia1 VHH (which has affinity for EGFR[30]) or 4F2 VHH (which has affinity for ZnO[20]) via a llama IgG2 upper hinge-linker (EPKIPQPQPKPQPQPQPQPQPKPQPKPEP).[31] The genes of the dimeric VHH fragments (Ia1-E32 and 4F2-E32) were generated by means of overlap extension PCR with LA-Taq DNA polymerase, and the gene fragments were inserted into the *Nco*I–*Sac*II sites of pRA-FLAG vectors (pRA-Ia1VHH-LH-AuE32VHH-FLAG and pRA-4F2VHH-LH-AuE32VHH-FLAG).

The DNA sequence coding one of the selected VHH genes (E32 clone) with the IgA hinge linker (SPSTPPTPSPSTPP) and a biotin acceptor peptide (Avitag; GGLDNDIFEAGKIEWH) at the C-terminus of VHH in that order (as reported by Cloutier et al.[32]) was generated by overlap extension PCR from the pRA-FLAG vector containing the E32 VHH fragment (pRA-AuE32VHH-FLAG), and the amplified fragments were inserted into the *Nco*I–*Spe*I restriction sites of the pRA-FLAG vector (pRA-AuE32VHH-Avitag).

Expression and Purification of VHH Fragments. Transformed *E. coli* BL21 (DE3) cells harboring the expression plasmid encoding the VHH and dimeric VHH fragments were incubated in 2 × yeast extract tryptone medium containing 100 g/mL ampicillin at 28 °C, and expression of antibody fragments under the control of the T7 promoter was induced by adding 1 mM isopropyl β-D-thiogalactopyranoside. VHH fragments were

dx.doi.org/10.1021/bc300316p | *Bioconjugate Chem.* 2012, 23, 1934–1944

Table 1. Amino Acid Sequences of CDR Loops of GBP-Grafted VHH Fragments[b]

Fragment	CDR1	CDR2	CDR3
	26 35c	50 65	95 102
cAbBCII10	GGSEYS-YSTF SLG	AIASM--GGLTYYADSVK-G	VRGYFMRLPSSHNFRY
	1-1 1-18	50 65	95 102
VHH_{GBP1}	GGSLKAHLPPSRLPSSLG	AIASM--GGLTYYADSVK-G	VRGYFMRLPSSHNFRY
	1-1 1-18	50 65	3-1 3-16
Randomized VHH_{GBP1}[a]	GGSLKAHLPPSRLPSSLG	AIASM--GGLTYYADSVK-G	VRGαββαββαββαFRY

[a] α and β in CDR3 of randomized VHH_{GBP1} were randomized to R or H and R, G, L, or V, respectively. [b] The sequence of the GBP is underlined. The numbering of the amino acids of cAbBCII10 VHH follows the Kabat numbering system.[33] The amino acids of the GBP-grafted CDR1 and randomized CDR3 are numbered as 1-1 to 1-18 and 3-1 to 3-16, respectively.[20]

extracted from the periplasm of the harvested cells by osmotic shock and were purified by anion/cation exchange chromatography and gel filtration chromatography (Hi-Load 16/600 Superdex 75 size exclusion column, GE Healthcare, Little Chalfont, UK) after treatment with ammonium sulfate. The bispecific VHH dimers were first purified by means of affinity chromatography on an anti-FLAG M2 affinity gel column (Sigma, Tokyo, Japan) and then fractionated by gel filtration chromatography.

For the expression of biotinylated VHH fragments, *E. coli* BL21 (DE3) cells were transformed by the plasmid of pBIRAcm encoding biotin ligase (Avidity Inc., Aurora, CO, USA), and then the same cells were transformed by the plasmids of pRA-AuE32VHH-Avitag. The transformed *E. coli* cells were incubated in 2 × yeast extract tryptone medium containing 100 μg/mL ampicillin and 34 μg/mL chloramphenicol at 28 °C. Expression of biotinylated VHH and biotin ligase was induced by adding 1 mM isopropyl β-D-thiogalactopyranoside in the presence of 50 μM of D-biotin (Sigma, St. Louis, MO, USA). VHH fragments were extracted from the periplasm of the harvested cells by osmotic shock and purified by means of affinity chromatography on a SoftLink Soft Release Avidin Resin column (Promega, Madison, WI, USA) and gel filtration chromatography. The fractionated biotinylated VHH was collected after the presence of biotin was confirmed in the proteins by means of Western blotting using streptavidin–horseradish peroxidase (GE Healthcare).

Analysis of Binding Affinities and Specificity of VHH Fragments for Gold Surfaces. Gold powder (6 mg) was added to 300 μL of 10 mM phosphate solution (pH 7.5; 200 mM NaCl, 0.05% Tween 20) containing VHH, and the solution was incubated for 30 min at 4 °C. After the solution was centrifuged at 20000*g* for 10 min, the amount of unbound VHH in the supernatant was measured by means of the bicinchoninic acid method with a Micro BCA Protein Assay Reagent Kit (Pierce Biotechnology, Rockford, IL, USA). The amount of protein adsorbed on the gold powder was calculated by subtracting the amount of unbound protein from the total amount of VHH used.

For analysis of the specificity of the VHH fragments for gold surfaces, commercially available gold, platinum, palladium, and silver plates (Nilaco, Tokyo, Japan) were soaked for 30 min in 10 mM phosphate solution (pH 7.5; 200 mM NaCl, 0.1% Tween 20) containing the VHH fragments with a FLAG tag. The plates were washed three times with the same phosphate solution without VHH and then soaked in a solution of mouse anti-FLAG M2 antibody (pH 7.5; 10 mM phosphate, 200 mM NaCl, 0.1% Tween 20). The plates were washed again three times, and the chemiluminescence from peroxidase conjugated to the anti-mouse antibody was observed on the plates.

Suppression of Gold Nanoparticle Aggregation by Gold-Binding VHH Fragments. A solution of gold nanoparticles (size 20 nm; Sigma-Aldrich, Tokyo, Japan) was dialyzed against 10 mM phosphate solution (pH 7.5). To the gold nanoparticle solution, bovine serum albumin (BSA, Sigma-Aldrich) or E32 VHH was added such that the concentrations of the nanoparticles and the protein were 0.1 nM and 40 nM, respectively, at various NaCl concentrations. The absorption spectra of the gold nanoparticle solutions were measured with a U-3000 spectrophotometer (Hitachi, Tokyo, Japan) every 30 min for 360 min, and the difference between the molar extinction coefficients at 523 and 630 nm ($\Delta\varepsilon_{523-630}$) was traced.

SPR Scattering Imaging of Carcinoma Cells Overexpressing EGFR. Gold nanoparticle solutions (size 41.6 nm; Tanaka Kikinzoku Kogyo, Tokyo, Japan) were dialyzed against 10 mM phosphate solution (pH 7.5), and Ia1-E32 VHH dimers were added to the 0.2 nM solution of gold nanoparticles to bring the dimer concentration to 1 μM. The solution of the nanoparticles and dimers was added to 1.0×10^4 Chinese hamster ovary cells and A431 cancerous cells. The cells were incubated for 15 min and washed with 10 mM phosphate solution (pH 7.5). SPR scattering images of the washed cells were obtained with an inverted Olympus IX81 microscope (Olympus, Tokyo, Japan) with a dark field condenser (U-DCW). A UPLFLN 100×O2 objective lens was used to collect only the scattered light from the samples.

Assembly of Gold Nanoparticles from Gold-Binding VHH Tetramers. A 36 μM solution of the E32 VHH fragments with the biotin tag at the C-terminus was mixed with 9 μM streptavidin to form E32 VHH tetramers. The tetramerization of E32 VHH was confirmed by gel filtration chromatography (Superdex 200 10/300 size exclusion column, GE Healthcare, Little Chalfont, U.K.). VHH tetramers at various concentrations were mixed with 0.1 nM gold nanoparticles in a 10 mM phosphate solution (pH 7.5). The $\Delta\varepsilon_{523-630}$ values were measured every 30 min for 540 min to observe the aggregation of the gold nanoparticles.

Linkage of Gold and ZnO Nanoparticles via Bispecific VHH Dimers. A 10 mM phosphate solution (1 mL, pH 7.5;

Table 2. Sequences of VHH Fragments after Four Rounds of Selection against Gold Particles[a]

Fragment	CDR3	Number of clones among 100 colonies
	3-1 3-16	
E3 VHH	VRGRRVRGGRLLHFRY	4
E9 VHH	VRGRRVRGGHVLRFRY	4
E12 VHH	VRGRRVRGGRVLRFRY	3
E32 VHH	VRGRRVRGGHLLRFRY	3

[a]Selected sequences are underlined. The amino acids of CDR3 in the selected VHH fragments are numbered as 3-1 to 3-16.[20]

200 mM NaCl) containing 40 μg of ZnO particles (~100 nm; Hosokawa Micron Inc., Hirakata, Japan) was sonicated for 1 min. E32 VHH, 4F2 VHH, and 4F2-E32 dimers were added to the suspension at various concentrations, and then 20 nm gold nanoparticles were added at a final concentration of 0.2 nM. The solutions were centrifuged at 9500g for 5 s, and the absorption spectra of the supernatants were measured.

In addition, solutions of 40–400 μg/mL ZnO particles and 1 μM 4F2-E32 dimeric VHH fragments were allowed to stand for 3 h without centrifugation after the addition of 0.2 nM gold nanoparticles, for observation of spontaneous precipitation of gold and ZnO nanoparticles. In addition, after the gold nanoparticles were added, the solution was dried on collodion-coated 400 mesh copper grids for transmission electron microscopy with a LEO 912 AB OMEGA electron microscope (Carl Zeiss, Oberkochen, Germany) operating 100 kV.

RESULTS

Generation of High-Affinity Gold-Binding VHH Fragments. In CAnIGET method,[20] material-binding peptide is

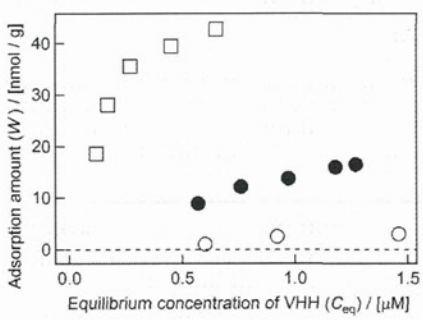

Figure 1. Adsorption isotherms for cAbBCII10 VHH (open circles), VHH_{GBP1} (filled circles), and E32 VHH (open squares) against 6 mg of gold particles in 10 mM phosphate solution (pH 7.5; 200 mM NaCl, 0.05% Tween 20).

replaced with one of three CDRs in VHH fragment and another CDR was randomized to select high-affinity VHH fragment by means of phage display approach. To generate VHH fragments with high affinity for gold surfaces, we replaced the CDR1 sequence in the VHH fragment of camel anti-BcII β-lactamase antibody cAbBCII10[33] with the sequence of a previously reported gold-binding peptide (GBP) (Table 1).[28] The CDR3 loop in the resulting GBP-grafted VHH fragment (VHH_{GBP1}) was randomized with the $\alpha\beta\beta\alpha$ repeating sequence format, where the α and β residues were randomized to Arg or His and to Arg, Gly, Leu, or Val, respectively; and the

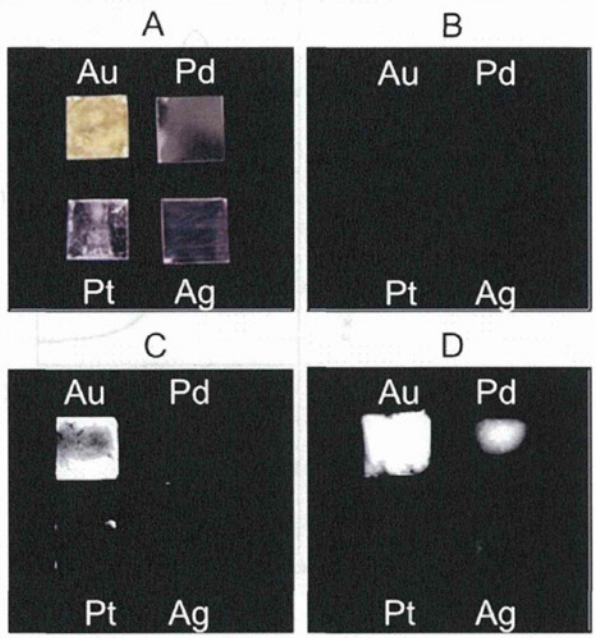

Figure 2. Specificity of VHH_{GBP1} and E32 VHH for material surfaces. Untreated gold, platinum, palladium, and silver plates (A) were soaked in a solution containing cAbBCII10 (B), VHH_{GBP1} (C), or E32 VHH (D), and then the residual VHH fragments with a FLAG tag at the C terminus on the plates were detected by the chemiluminescence from anti-mouse IgG antibody horseradish peroxidise.

randomized VHH fragments were displayed on filamentous bacteriophage M13. The phages were mixed with gold powder, and then the powder was washed with 50–200 mM phosphate solutions containing 0.05% Tween 20 to remove nonspecifically bound phages. Residual phages on the powder were eluted with a highly concentrated phosphate solution (500 mM), which inhibits protein adsorption on inorganic materials.[20,34] After four rounds of selection, we randomly picked 100 colonies and then compiled statistics for the frequency of amino acid residues at each position in CDR3 before selection and after four rounds of selection by analyzing the sequences of the chosen clones (Figure S1 in the Supporting Information). The statistical analysis showed the concentrations of specific amino acids at each position resulting from the molecular evolutional process. Several colonies had the same clones (E3, E9, E12, and E32), each of which had the same arginine-rich sequence (RRVRGG, Table 2). We attempted to estimate the gold-binding affinity of these four clones. However, only the E32

dx.doi.org/10.1021/bc300316p | Bioconjugate Chem. 2012, 23, 1934–1944

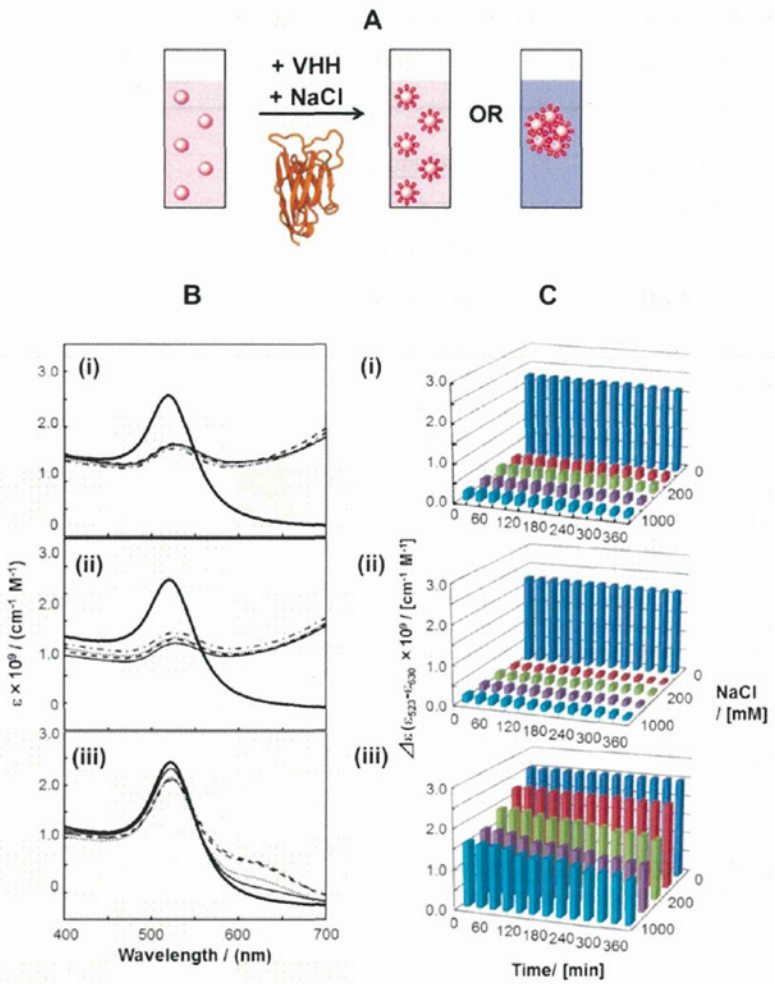

Figure 3. Suppression of gold nanoparticle aggregation by E32 VHH. (A) Experimental scheme for the analysis of aggregation suppression by VHH fragments. (B) Absorption spectra of 0.1 nM gold nanoparticles in 10 mM phosphate solution (pH 7.5) at NaCl concentrations of 0 M (bold solid line), 50 mM (solid line), 200 mM (dotted line), 500 mM (dashed line), and 1000 mM (dashed and dotted line), without protein (i), with 40 nM BSA (ii), and with 40 nM E32 VHH (iii). (C) Time dependence of the plasmon absorption at 520 nm from 0 to 360 min without protein (i), with 40 nM BSA (ii), and with 40 nM E32 VHH (iii) at NaCl concentrations of 0, 50, 200, 500, and 1000 mM.

clone was adequately expressed in *E. coli*, which was used for the binding assay; therefore, we measured the adsorption isotherms of the VHH_{GBP1} and E32 VHH fragments (Figure 1). Only small amounts of the cAbBCII10 VHH fragment were adsorbed on the gold particles (open circles in Figure 1), whereas the VHH_{GBP1} and E32 VHH fragments were bound with dissociation equilibrium constants (K_D) of 3 μM (close circles in Figure 1) and 150 nM (open squares in Figure 1), respectively: the affinity of E32 VHH was about 20 times that of VHH_{GBP1}. The grafting of material-binding peptide in CDR 1 functionalized the VHH fragment and the optimization of CDR3 sequence using phage display method promoted the affinity of the peptide-grafted VHH.

In addition, we also analyzed the affinity of VHH_{GBP1} and E32 VHH fragments for other inorganic materials. We soaked gold, palladium, platinum, and silver plates in a solution containing VHH fragments bearing a FLAG tag at the C termini. After washing the plates, we detected residual VHH fragments on the plates by measuring the chemiluminescence from horseradish peroxidase conjugated with anti-mouse Fc antibody via anti-FLAG M2 mouse antibody. Selective adsorption of the VHH_{GBP1} and E32 VHH fragments on the gold surface was clearly observed, although E32 VHH also bound weakly to palladium (Figure 2). These results indicate that the binding functionalities of VHH_{GBP1} and E32 VHH were selective for gold surfaces.

Suppression of Gold Nanoparticle Aggregation under High-Ionic-Strength Conditions by E32 VHH Fragments. We used the E32 VHH fragments to suppress gold nanoparticle aggregation in aqueous solution as follows. E32 VHH fragments (40 nM) were added to 10 mM phosphate (pH 7.5) solution containing 0.1 nM gold nanoparticles (size: 20 nm, Figure 3A). We chose the 1:400 molar ratio of gold nanoparticles to E32 VHH because at least 400 molecules of E32 VHH are required for complete coverage of the surface of 20 nm gold nanoparticles. A solution of 20 nm gold nanoparticles generally has a plasmon absorption at around 520 nm; however, the nanoparticles aggregate easily as the ionic strength is increased, and as a result, the plasmon absorption is red-shifted from the red to the purple region. Here, we

dx.doi.org/10.1021/bc300316p | *Bioconjugate Chem.* 2012, 23, 1934−1944

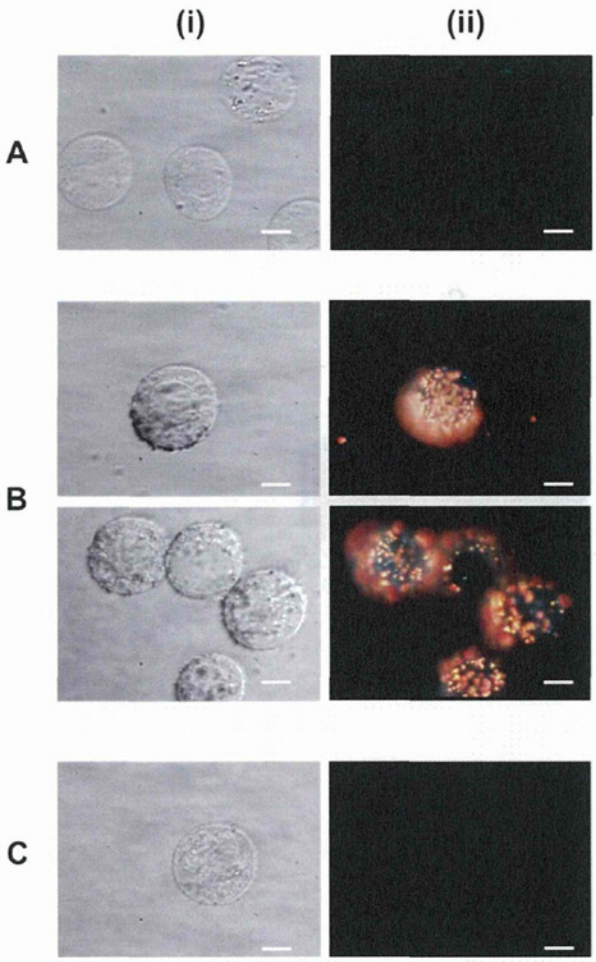

Figure 4. Micrograph (i) and surface plasmon resonance (SPR) scattering image (ii) of A431carcinoma cells with 0.2 nM gold nanoparticles (A), A431carcinoma cells with 1 μM VHH dimer and 0.2 nM gold nanoparticles (B), and CHO noncarcinoma cells with 1 μM VHH dimer and 0.2 nM gold nanoparticles (C). SPR scattering images were obtained by using a dark-field condenser. Gold color shows SPR scattering of gold particles. Scale bars = 10 μm.

observed that the plasmon absorption band of 0.1 nM gold nanoparticles in 10 mM NaCl (data not shown) was red-shifted relative to the band in the absence of NaCl, and the band disappeared when the NaCl concentration was increased to 50 mM in the absence of detergents (Figure 3Bi). Bovine serum albumin (BSA) is often used to inhibit nanoparticle aggregation,[35,36] and the molecular weight (BSA: ~60 kDa) is larger than that of VHH (~15 kDa); however, 40 nM BSA only slightly suppressed the aggregation of gold nanoparticles in 50 mM NaCl solution (Figure 3Bii). In contrast, the addition of 40 nM E32 VHH markedly suppressed aggregation even in 1000 mM NaCl solution (Figure 3Biii). Evaluation of the time dependence of the plasmon absorption at 520 nm at various NaCl concentrations indicated that E32 VHH suppressed the aggregation of gold nanoparticles for 6 h (Figure 3C). Although the plasmon absorption intensity decreased slightly with time at NaCl concentrations exceeding 200 mM even in the presence of E32 VHH, E32 VHH markedly suppressed gold nanoparticle aggregation at all the tested NaCl concentrations.

One-Pot Biofunctionalization of Gold Nanoparticles. Gold nanoparticles can resonantly scatter visible light when their surface plasmon oscillation is excited.[26] Here, we functionalized gold nanoparticles with bispecific VHH dimers with affinity for both EGFR and gold surfaces, for use in cellular imaging by means of SPR scattering. One advantage of working with antibodies is the ability to use various fusion technologies. E32 VHH was fused at the C-terminus of Ia1 VHH with affinity for EGFR[30] via a llama IgG2 upper hinge-linker,[31] and bispecific antibody with affinity for gold and EGFR (Ia1-E32 VHH) was constructed. In the absence of the Ia1-E32 VHH dimer, no SPR scattering was detected on A431 cancerous cells that overexpress EGFR (Figure 4A). In contrast, in the presence of the Ia1-E32 VHH dimer, clear SPR scattering by gold nanoparticles was detected on the cancerous cells (Figure 4B). In addition, we added gold nanoparticles functionalized with Ia1-E32 VHH dimers to Chinese hamster ovary cells on which no EGFRs were expressed; in this case, no SPR scattering from gold nanoparticles was observed even in the presence of the Ia1-E32 VHH dimer (Figure 4C). These results indicate that the dimer interlinked the gold nanoparticles and the EGFR-displaying cancerous cells. The dimer simultaneously stabilized and biofunctionalized the gold nanoparticles.

Construction of Biointerfaces between Nanomaterials. To demonstrate that material-binding camel antibody fragments could serve as biointerfaces between nanomaterials, we constructed E32 VHH tetramers by taking advantage of the biotin–avidin interaction (Figure 5A). E32 VHH fragments (36 μM) with the biotin acceptor peptide fused at the C-termini were mixed with 9 μM streptavidin, and the resulting E32 VHH tetramers were fractionated by size exclusion chromatography (Figure S2 in the Supporting Information). Then the tetramers were added at various concentrations to a 0.1 nM solution of gold nanoparticles in the absence of NaCl. When the tetramer concentration was <20 nM, the plasmon intensity at 520 nm decreased, but no red-shift was observed (Figure 5Bi,ii). However, when the tetramer concentration was >40 nM, the plasmon band was red-shifted (Figure 5Biii,iv), and the plasmon absorption intensity decreased rapidly with time (Figure 5C). These results indicate that the tetramers acted as interface molecules between the gold nanoparticles and that the nanoparticles spontaneously aggregated via the tetramers.

To use a material-binding VHH as a biointerface between different nanomaterials, we also designed bispecific VHH dimers from E32 VHH and a ZnO-binding VHH (4F2 VHH)[20] by fusing E32 VHH at the C-terminus of 4F2 VHH via a hinge-linker. When we centrifuged a suspension containing 0.2 nM gold nanoparticles (20 nm) and 40 μg/mL ZnO particles (~100 nm) with the E32 VHH or 4F2 VHH monomer, only ZnO particles precipitated; as a result, the supernatant had the same plasmon absorption intensity before centrifugation (open and closed circles in Figure 6). In contrast, when bispecific 4F2-E32 VHH dimers were added to the mixture of gold and ZnO particles, the plasmon absorption intensity decreased with increasing dimer concentration (open squares in Figure 6): the plasmon absorption intensity of the gold nanoparticles decreased at a dimer concentration of 40 nM, and complete precipitation of gold and ZnO nanoparticles was observed when the dimer concentration exceeded 500 nM. These results indicate that the 4F2-E32 VHH dimers linked the gold and ZnO particles and induced the precipitation of gold nanoparticles with ZnO.

dx.doi.org/10.1021/bc300316p | *Bioconjugate Chem.* 2012, 23, 1934–1944

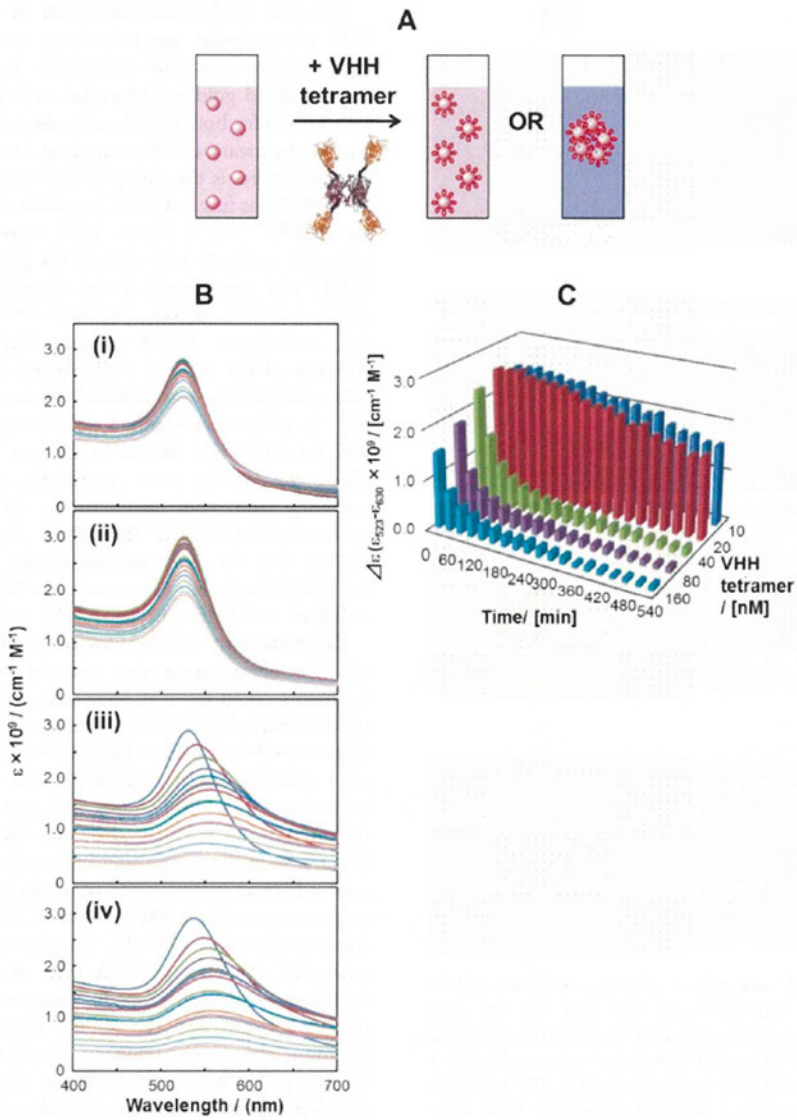

Figure 5. Functionalization of gold nanoparticles with a VHH tetramer. (A) Experimental scheme for functionalization by the VHH tetramer. (B) Time dependence of the absorption spectra of 0.1 nM gold nanoparticles in 10 mM phosphate (pH 7.5) in the presence of 10 nM (i), 20 nM (ii), 40 nM (iii), and 80 nM (iv) VHH tetramer in the absence of NaCl. The spectra were collected every 30 min for 540 min. (C) Aggregation behavior of gold nanoparticles upon addition of the VHH tetramer at various concentrations.

We also observed spontaneous precipitation of gold and ZnO particles in the presence of bispecific 4F2-E32 VHH dimers. We observed no change in a gold nanoparticle solution when ZnO particles were added in the absence of the bispecific dimers; whereas in the presence of dimers (1 μM), the addition of ZnO particles resulted in an immediate change in color of the solution from red to purple, and gold and ZnO particles spontaneously precipitated (Figure 7Ai). Spontaneous precipitation in the presence of bispecific VHH dimers was also observed when the amount of added ZnO particles was increased to 400 μg, and the particle aggregation rate was accelerated (Figure 7Aii).

The ZnO suspensions just after gold nanoparticles were added were dried on collodion-coated grids for transmission electron microscopy (Figure 7B). No gold nanoparticles were observed on the ZnO particles in the absence of the VHH dimer, whereas many gold nanoparticles were observed on the ZnO particles in the presence of the VHH dimer. These results indicate that the bispecific 4F2-E32 VHH dimers linked the ZnO and gold nanoparticles and induced spontaneous precipitation of both types of nanoparticles.

DISCUSSION

Generation of VHH Fragments with High Affinity and Specificity for Gold Surfaces. Antibodies are naturally occurring proteins with excellent molecular recognition in the immune system, and they have been widely used in medical, sensing, and imaging applications.[37,38] A few antibodies that can bind inorganic material surfaces have been identified,[24,39,40] but the number of material-binding antibodies is far lower than the number of material-binding peptides because of the low immunogenic potential of inorganic materials. Even when in

dx.doi.org/10.1021/bc300316p | Bioconjugate Chem. 2012, 23, 1934−1944

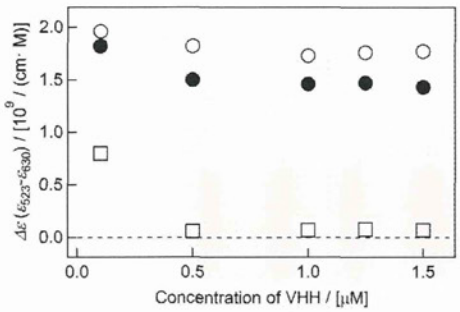

Figure 6. Absorption intensity of the plasmon band at 520 nm in the supernatant of a mixture of gold and ZnO nanoparticles at various concentrations (0.1, 0.5, 1.0, 1.25, and 1.5 μM) of E32 VHH (open circles), 4F2 VHH (filled circles), and VHH dimer (open squares) after centrifugation.

vitro selection methods are used, the fact that antibody fragments have higher molecular weights than peptides limits the library diversity. Previously, Barbas et al. generated the human antibody fragments with affinity for integrins by a combination of peptide grafting and in vitro selection: the sequence of the integrin-binding tripeptide (Arg-Gly-Asp) was grafted in a CDR, and the conformation of the grafted CDR was optimized by in vitro selection.[41] On the basis of their concept (a combination of peptide grafting and in vitro selection), we, recently, proposed the CAnIGET approach and conveniently generated the antibody fragments with high affinity for ZnO, CoO, and Al_2O_3 surfaces.[20,23] This method involves the application of the variable domain of a camel VHH, which is a simple single domain, as a scaffold for peptide grafting. The VHH domain is functionalized by replacing one CDR loop with a material-binding peptide and randomizing another CDR loop and selecting high-affinity fragments.

In this study, we grafted a previously reported gold-binding peptide sequence of GBP into the CDR1 loop of cAbBCII10 and selected high-affinity VHH fragments from a library in which the CDR3 loop of VHH_{GBP1} was randomized with an $\alpha\beta\beta\alpha$ motif (Arg or His at the α position, and Arg, Gly, Leu, or Val at the β position). After the selection of high-affinity clones, a specific amino acid was selected at each position. Interestingly, Arg was predominantly selected at the α positions (Figure S1 in the Supporting Information), and four clones (E3, E9, E12, and E32) found in several colonies among the 100 colonies that were chosen had the same Arg-rich alignment sequence (RRVRGG, Table 2). A His residue has been found in many previously reported material-binding peptides, but a study of the use of homopolypeptides for the adsorption on gold surfaces suggested that Arg and Thr residues have an affinity for gold surfaces.[42] This suggestion supports the preferred selection of Arg in CDR3 that we observed in this study.

Both VHH_{GBP1} and E32 VHH had specificity for gold surfaces (Figure 2C,D). This result supports our previous suggestion that the specificity of a selected VHH for inorganic materials depends on the peptide grafted into CDR1.[20] Recently, we identified a fragment of variable region (Fv) of a human antibody, A14P-b2, with affinity and specificity for gold surfaces from a phage-displayed library of a human antibody library.[24] The fragment was used for specific patterning of proteins and for an immunoassay on a gold-patterned substrate.[24] However, the fact that the human Fv is a heterodimer composed of the variable regions of the heavy chain (VH) and light chain (VL) complicates the design of bispecific molecules, such as diabodies and tandem single-chain Fvs (scFvs);[43] consequently, the preparation of bispecific antibodies in bacteria is often difficult. Previously, we used only the VH domain of A14P-b2 to generate a bispecific molecule by fusing the VH at the terminus of an antilysozyme scFv, and we demonstrated the use of the VH-scFv molecule for an immunoassay.[19,44] However, isolated VH domains tend to aggregate.[45] In the current study, we generated a gold-binding VHH fragment, which is a simple single domain and is stable even without the light chain fragment, and we expected that bispecific molecules generated with the VHH would be more stable.

One-Pot Functionalization of Gold Nanoparticles by Means of Gold-Binding VHH Fragments. Gold nanoparticles strongly absorb and scatter visible and near-infrared light by means of plasmon resonance.[2,25,26] The optical properties of nanoparticles depend on their size and colloidal stability, and they can be used as probes for sensing[25] and imaging[26] applications. The colloidal stability of gold nanoparticles is determined by the balance between van der Waals and electrostatic interactions.[46,47] Bare gold nanoparticles aggregate in response to small changes in ionic strength, owing to a decrease in electrostatic repulsion between particles that occurs upon binding of counterions to the particle surfaces. Surface modification with surfactants, polymers, or biomolecules can suppress the aggregation.[48]

Chemical coupling between gold and thiol groups has been often used to conjugate organic molecules to gold nanoparticle surfaces.[48] Proteins can be conjugated to the nanoparticles if the organic molecule linker has an appropriate functional group at the terminus opposite to the thiol group. However, the series of reactions required to generate such biofunctionalized gold nanoparticles is complicated, and it often reduces the activity of the immobilized proteins because the method cannot offer control of protein orientation at the surface and get around denaturation of proteins.[49] Here, we performed one-pot functionalization of gold nanoparticles by using the high-affinity, high-specificity interaction of material-binding antibody fragments with material surfaces. We obtained high-affinity E32 VHH fragments that spontaneously bound to gold nanoparticles and suppressed nanoparticle aggregation even in a high-ionic-strength solution. In addition, the simple single-domain structure of the VHH enabled us to design bispecific dimers by fusing different VHH fragments at the N-terminus of E32 VHH. For example, an anti-EGFR VHH was orientationally immobilized on gold nanoparticles in a single step.

In general, to obtain biofunctional nanoparticles for sensing and imaging, IgG-type antibodies with molecular weights of ~150 kDa (15 nm) are conjugated to gold nanoparticles. Conjugating several antibodies on a single nanoparticle is generally difficult. However, because the VHH dimers used in this study (~30 kDa) were much smaller than IgG type antibodies, the antigen-binding domains could be more efficiently and densely conjugated on the gold nanoparticles. The resulting functionalized nanoparticles can be expected to be useful for diagnostic applications such as gold labeling[50,51] and photothermal therapy involving gold nanorods.[52]

High-Affinity VHH Fragments as Interface Molecules. Although nanomaterials that have strictly controlled shapes and disperse completely in solution can self-assemble by means of two-dimensional crystallization,[7,8] interface linkers that act as a

dx.doi.org/10.1021/bc300316p | Bioconjugate Chem. 2012, 23, 1934–1944

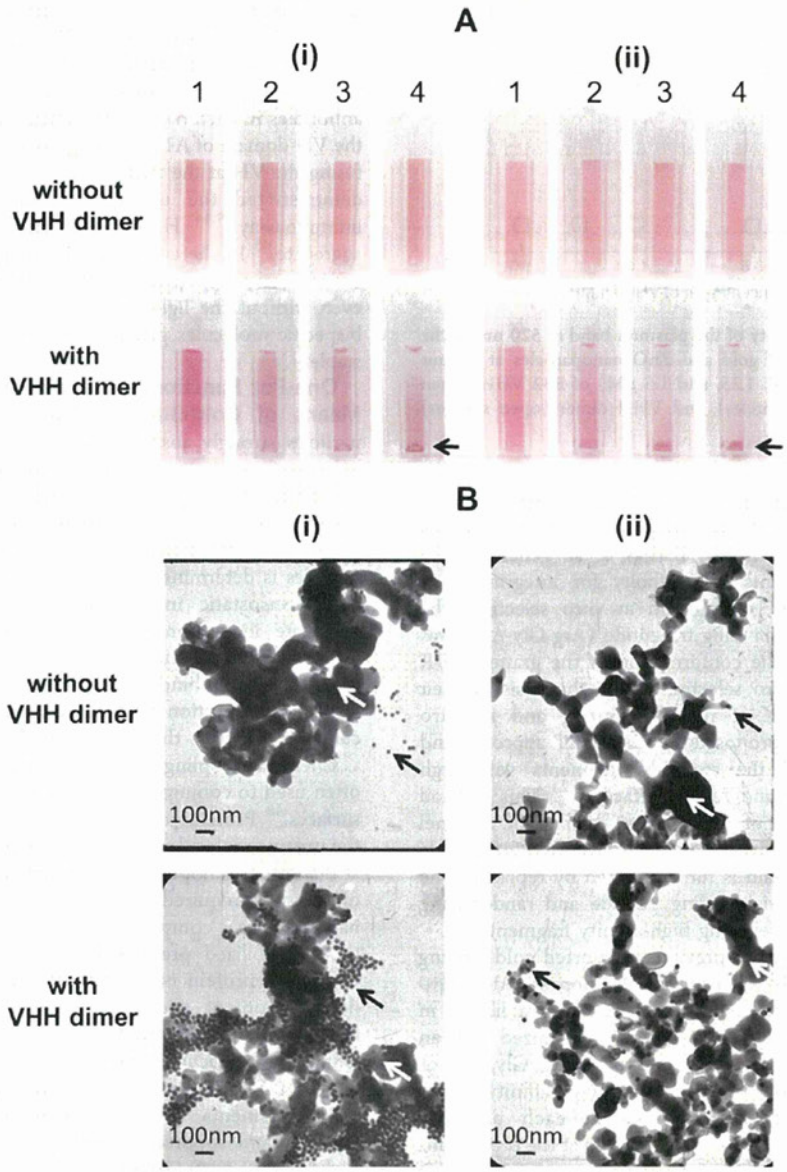

Figure 7. (A) Photographs showing spontaneous precipitation before the addition of 1 μM VHH dimer (1) and 60 min (2), 120 min (3), and 180 min (4) after addition of the dimer. (B) Transmission electron microscopy images of the mixture of gold nanoparticles (0.2 nM) and ZnO nanoparticles: 40 μg/mL (i) and 400 μg/mL (ii).

glue between different nanomaterials can facilitate complicated bottom-up assembly of nanodevices. Biomolecules such as nucleic acids and polypeptides are among the most attractive linkers because of their high specificity. For example, DNA–DNA,[53] biotin–avidin,[54,55] and antigen–antibody[56] interactions have been used to mediate self-assembly of nanomaterials by covalently conjugating the biomolecules on nanoparticles. In this study, we generated biomolecules with direct affinity for the surface of inorganic nanoparticles, which obviated the need for the fabrication of nanoparticle surfaces with specific functional groups for conjugating biomolecules. Many peptides with affinity for inorganic material surfaces have been identified by means of combinatorial approaches, and such peptides have been used for the patterning of nanoparticles and proteins on films.[13,57,58] However, there have been fewer reports on the use of material-binding peptides to link nanoparticles because the binding affinity of such peptides is not sufficient to overcome electrostatic interactions between nanoparticles or the Brownian motion of nanoparticles.[47,48] Here, we generated high-affinity gold-binding antibody fragments, and we used some previously reported structural formats of various multivalent and multispecific antibodies[43] to create tetravalent antibodies from gold-binding VHH fragments and bispecific VHH dimers by fusing a ZnO-binding VHH with a gold-binding VHH. These multivalent and multispecific antibody fragments spontaneously linked two different types of nanoparticles (gold–gold, gold–ZnO). Our results demonstrate the potential of high-affinity multivalent and bispecific antibodies to act as glues between nanomaterials.